POLITECNICO DI TORINO
Repository ISTITUZIONALE

Multiscale characterization of Ti-induced grain refinement in additively manufactured austenitic stainless steel

Original
Multiscale characterization of Ti-induced grain refinement in additively manufactured austenitic stainless steel / Jandaghi, M.R., Pouraliakbar, H., Shim, S.H., Iannucci, L., Tarafder, P., Palisaitis, J., Hong, S.I., Persaud, S.Y., Fallah, V., Calmunger, M., Moverare, J.. - In: MATERIALS & DESIGN. - ISSN 0264-1275. - ELETTRONICO. - 261:(2026), pp. 1-20. [10.1016/j.matdes.2025.115192]

Availability:
This version is available at: 11583/3006888 since: 2026-01-23T11:52:51Z

Publisher:
Elsevier

Published
DOI:10.1016/j.matdes.2025.115192

Terms of use:

This article is made available under terms and conditions as specified in the corresponding bibliographic description in the repository

Publisher copyright

(Article begins on next page)

14 September 2026

Materials & Design 261 (2026) 115192

Contents lists available at ScienceDirect

Materials & Design

journal homepage: www.elsevier.com/locate/matdes

Multiscale characterization of Ti-induced grain refinement in additively manufactured austenitic stainless steel

Mohammad Reza Jandaghi [a,b,*], Hesam Pouraliakbar [c], Sang Hun Shim [d], Leonardo Iannucci [e], Prithwish Tarafder [a], Justinas Palisaitis [f], Sun Ig Hong [g], Suraj Y. Persaud [h], Vahid Fallah [c], Mattias Calmunger [a], Johan Moverare [a,b]

[a] Division of Engineering Materials, Linköping University, 581 83 Linköping, Sweden
[b] Wallenberg Initiative Materials Science for Sustainability, Department of Management and Engineering (IEI), Linköping University, Linköping SE-58183, Sweden
[c] Azar Advanced Manufacturing Laboratory (AAML), Department of Mechanical and Materials Engineering, Queen's University, Kingston, ON K7L 3N6, Canada
[d] Extreme Materials Research Institute, Korea Institute of Materials Science (KIMS), Changwon, the Republic of Korea
[e] Department of Applied Science and Technology, Politecnico di Torino, Corso Duca Degli Abruzzi 24, 10129 Torino, Italy
[f] Thin Film Physics Division, Department of Physics, Chemistry and Biology (IFM), Linköping University, SE-581 83 Linköping, Sweden
[g] Department of Materials Science and Engineering, Chungnam National University, Daejeon 34134, the Republic of Korea
[h] Department of Mechanical and Materials Engineering, Queen's University, Kingston, ON K7L 3N6, Canada

ARTICLE INFO

Keywords:
Additive manufacturing
Laser powder bed fusion (LPBF)
In-situ alloying
Grain refinement
316L stainless steel
Laves phase

ABSTRACT

In-situ inoculation of grain-refining elements can effectively mitigate columnar grain growth and alleviate mechanical anisotropy in additively manufactured metals, while enhancing strength via the Hall-Petch effect. However, the refinement mechanism of Ti in austenitic stainless steel remains unclear. This study investigates Mn-assisted Ti inoculation in 316L stainless steel (SS316L), followed by annealing. Despite near-full densification, localized Ti enrichment formed coarse, brittle FeTi and C14 Laves intermetallic clusters, encapsulated by ultrafine ferritic grains within an austenitic matrix. Elevated annealing temperatures dissolved Laves phases and promoted Ti diffusion, resulting in dispersed TiO particles and ferritic domains. Refined Laves phases were redistributed to grain boundaries and triple junctions. Mechanical testing showed improved ductility with increasing annealing temperature: ultimate tensile strength decreased from 650 MPa to 610 MPa, while elongation rose from 13 % to 38 %. Hardness mapping revealed a more uniform distribution, though the maximum hardness dropped from 370 HV to 210 HV. Electrochemical corrosion tests in saline solution indicated that phase transformations induced by Ti-Mn co-inoculation undermined the corrosion resistance of SS316L, rendering it more susceptible to degradation in aggressive environments.

1. Introduction

Fusion-based additive manufacturing (AM) of metals typically yields columnar grain structures, resulting in anisotropic mechanical properties and limiting component performance [1]. This morphology arises from unidirectional heat flow during solidification, with grain growth kinetics and texture governed by heat dissipation rate and anisotropy [2]. Among AM techniques, laser powder bed fusion (LPBF) offers high resolution and dimensional accuracy, but its rapid cooling rates complicate grain control and increase hot-cracking susceptibility [3,4]. LPBF also introduces significant residual stresses, causing distortions post-build or during service [5]. Attempts to induce columnar-to-equiaxed transition (CET) by adjusting process parameters have shown limited success [6,7]. Instead, incorporating grain-refining phases has proven more effective in lowering nucleation barriers and promoting equiaxed grains [8]. These phases typically exhibit low lattice mismatch (<5%) with the matrix [9–11], and nucleate at minimal undercooling. Grain-refiner elements like Zr, Sc, Ti, and B can be added ex-situ via pre-alloying or in-situ through feedstock mixing and inoculation [12,13]. Pre-alloyed powders ensure homogeneity, while in-situ alloying offers cost-effective composition tuning by bypassing casting and atomization [14]. However, in-situ approaches may introduce microstructural heterogeneity [15]. In AM, optimal parameters are those maximizing relative density; while for in-situ alloying, they must also ensure uniform

* Corresponding author at: Division of Engineering Materials, Linköping University, 581 83 Linköping, Sweden.
E-mail address: mohammadreza.jandaghi@liu.se (M.R. Jandaghi).

https://doi.org/10.1016/j.matdes.2025.115192
Received 11 July 2025; Received in revised form 30 October 2025; Accepted 20 November 2025
Available online 21 November 2025
0264-1275/© 2025 The Author(s). Published by Elsevier Ltd. This is an open access article under the CC BY license (http://creativecommons.org/licenses/by/4.0/).

dispersion of additions. Additive characteristics influence LPBF phenomena such as laser absorption, heat flow, and vaporization. Thus, selecting suitable grain-refining agents requires understanding their thermodynamic and kinetic interactions with the host alloy [16]. Recent studies have incorporated Ti (elemental or compound) into steels via in-situ AM, where Ti-bearing phases enhance grain refinement and strength, often preserving ductility via the Hall-Petch effect [17]. TiC nanoparticle additions to SS316L via LPBF showed improved strength and grain refinement, though agglomeration remained problematic [18–20]. Similar effects were observed with TiN in AISI 441 ferritic steel, attributed to CET via TiN-coated oxides [21]. Ikehata et al. reported TiO particles as nucleation sites in Fe and Fe-18Cr alloys, refining ferritic grains [22,23]. Though Laves phases were absent, SEM revealed secondary phases along grain boundaries (GBs), enclosing fine equiaxed grains in Fe-7.5Ti [23]. Zhai et al. [24] found that Ti agglomeration in SS316L via LPBF led to localized hardness doubling and brittle GB phases causing intergranular cracking. DED-based Ti addition followed by annealing produced undetectable EBSD phases and 1.5 times hardness increase [25]. Han et al. [25] attributed refinement to TiO_x particles, dismissing solute segregation. Grain refinement was also achieved by adding SS316L to (CP-Ti) [26] and Ti6Al4V [27], though EBSD revealed non-indexed martensitic α' lath regions. The role of Ti in stainless steels remains debated, as ferrite stabilizers like Ti, Cr, and Mo may promote sigma (σ) [28] and Laves [29] phases. While TiO_x formation is often cited, direct evidence is lacking. Given Ti's reactivity and agglomeration tendency in Cr/Mo-rich steels, concerns persist over undesired phase formation. This study aims to clarify the mechanisms of Ti-induced grain refinement, identifying phase evolution during in-situ alloying and post-treatment, and assessing their impact on microstructure, mechanical properties, and corrosion resistance.

2. Thermodynamic simulations

In-situ alloying alters the solidification pathway, influencing the alloy's vulnerability to solidification cracking [30]. This study utilized the TCFe7 database in Thermo-Calc™ to generate non-equilibrium Scheil solidification diagrams, modeling the liquid-to-solid transition [31]. The Scheil approach computes the solid fraction (f_S) as a function of temperature (T) and assesses cracking susceptibility via the slope of the $dT/d(f_S)^{1/2}$ curve near the solidification termination [32]. A steeper slope correlates with increased cracking risk [33,34]. The solid fraction is derived from the Scheil equation [35]:

$$f_s = 1 - \left(\frac{T_M - T}{T_M - T_L}\right)^{1/k-1} \quad (1)$$

Here, "T" denotes temperature, "T_M" the solvent's melting point, "T_L" the liquidus temperature. The partition coefficient "k" is defined as $k = C_s/C_L$ where the "C_S" and "C_L" are the solute concentrations in the solid and liquid phases, respectively.

In LPBF, rapid cooling rates steepen this gradient, curtailing solute redistribution and intensifying elemental segregation relative to equilibrium solidification [36]. Eutectic alloys, which undergo isothermal solidification, exhibit negligible $dT/d(f_S)^{1/2}$ slopes and superior printability due to their uniform liquid-to-solid transition and absence of a mushy zone. In contrast, solute additions that amplify the disparity between equilibrium and non-equilibrium solidification paths extend the solidification interval and enlarge the mushy zone, thereby exacerbating the risk of solidification cracking [37]. As shown in Fig. 1(a, b), the incorporation of 1 wt% Ti into SS316L markedly broadens the solidification range, elevating crack susceptibility during LPBF. Ti as a potent ferrite stabilizer, not only delays the BCC-to-FCC phase transformation but also facilitates the nucleation of the C14 Laves phase. To counterbalance these effects, 2 wt% Mn was introduced as an austenite stabilizer. Although Mn alone does not significantly narrow the solidification range, it promotes the BCC-to-FCC transition, as evidenced in Fig. 1(a, c). The synergistic addition of Mn and Ti reduces both the slope of the solidification curve (from 76° to 73°) and the solidification range (from 345 °C to 326 °C), thereby mitigating cracking propensity (Fig. 1 (b, d)). Furthermore, a comparative analysis of Fig. 1(a, b, d) confirms that Mn effectively offsets the Ti-induced retardation of the BCC-to-FCC transformation. Scheil simulations, however, do not account for local solute enrichment, which is prevalent in in-situ alloying. Ti agglomeration can locally promote direct solidification of Laves and Sigma phases, as indicated in Fig. 1(e). A detailed thermodynamic analysis of Gibbs free energy (ΔG_f) is essential for understanding phase evolution and guiding post-processing strategies. Heat maps **(**Fig. 1(f)**)** reveal that up to ~ 3 wt% Ti favors FCC_A1 formation, while ~ 10 wt% suppresses it and stabilizes BCC_A2. Controlled annealing can reduce Ti below 3 wt% and restore FCC stability. Ferrite persists up to 20 wt% Ti while Laves phases dominate beyond this point. In 10-20 wt% Ti regions, both may coexist. High-temperature annealing is needed to homogenize and redistribute Ti, reduce its concentration below 10 wt%, and suppress Laves phase formation.

To evaluate the Laves phase predicted by thermodynamic simulations, it is essential to examine the Fe-Ti binary system, which comprises two stable intermetallics at room temperature: FeTi and Fe_2Ti. FeTi crystallizes in a BCC structure with a lattice parameter closely matching ferrite, while Fe_2Ti adopts a C14 Laves phase with a hexagonal close-packed (HCP) configuration. Both phases are characterized by high hardness and brittleness and often exhibit non-stoichiometric compositions due to elemental substitutions from SS316L. Prior studies indicate that Cr can fully substitute Fe above 823 K, transforming C14 into C15 and C36 structures. Mn replaces Fe at 1273 K, with a homogeneity range of 30-41 at.% Ti. Ni can substitute Fe up to 20 at.% between 1173-1273 K, while Mo fully replaces Ti in Fe_2Ti and partially in FeTi (up to 2 at.% at 1173 K). Heat maps suggest Sigma phase formation at Ti concentrations between 3-20 wt%, with stability from room temperature to ~ 600 °C. Although equilibrium solidification disfavors Sigma due to earlier phase nucleation, rapid cooling and Ti agglomeration during LPBF promote its emergence. Mn has been shown to distribute uniformly in the melt, suppress Mo activity, and substitute Mo in Sigma, thereby destabilizing the phase [38]. Previous work confirmed Sigma phase presence in Ti-rich regions under high solidification rates [39]. While thermodynamic models predict phase stability based on temperature, transformation kinetics are time-dependent. To suppress Sigma formation, simulations recommend isothermal annealing above 700 °C. Accordingly, in-situ alloyed samples were annealed at 850 °C, 1050 °C, and 1250 °C for 1 h to mitigate undesirable phase evolution induced during printing.

3. Experimental methods

3.1. Materials

Gas-atomized SS316L powder (15-50 μm) sourced from Höganäs, Sweden, was blended with 1 wt% Ti (15-45 μm) and 2 wt% Mn (5-30 μm), both procured from Sigma-Aldrich, Germany, to prepare the LPBF in-situ alloying feedstock. The mixture was dried at 80 °C for 2 h. Fig. 2 presents a stereo-micrograph, SEM image, and EBSD inverse pole figure (IPF) of the SS316L powder, along with SEM and EDS maps of the blended feedstock.

3.2. Sample fabrication

Samples were fabricated on SS304L substrates using an LPBF system equipped with a 300 W ytterbium fiber laser (λ = 1064 nm), featuring a Gaussian energy profile and a 40 μm spot size. Argon shielding maintained oxygen levels below 100 ppm. Optimized parameters (90 W laser power, 400 mm/s scan speed, 30 μm layer thickness, 70 μm hatch spacing, and 67° interlayer rotation) achieved a relative density of 99.7 %. To evaluate thermal effects, specimens underwent isothermal

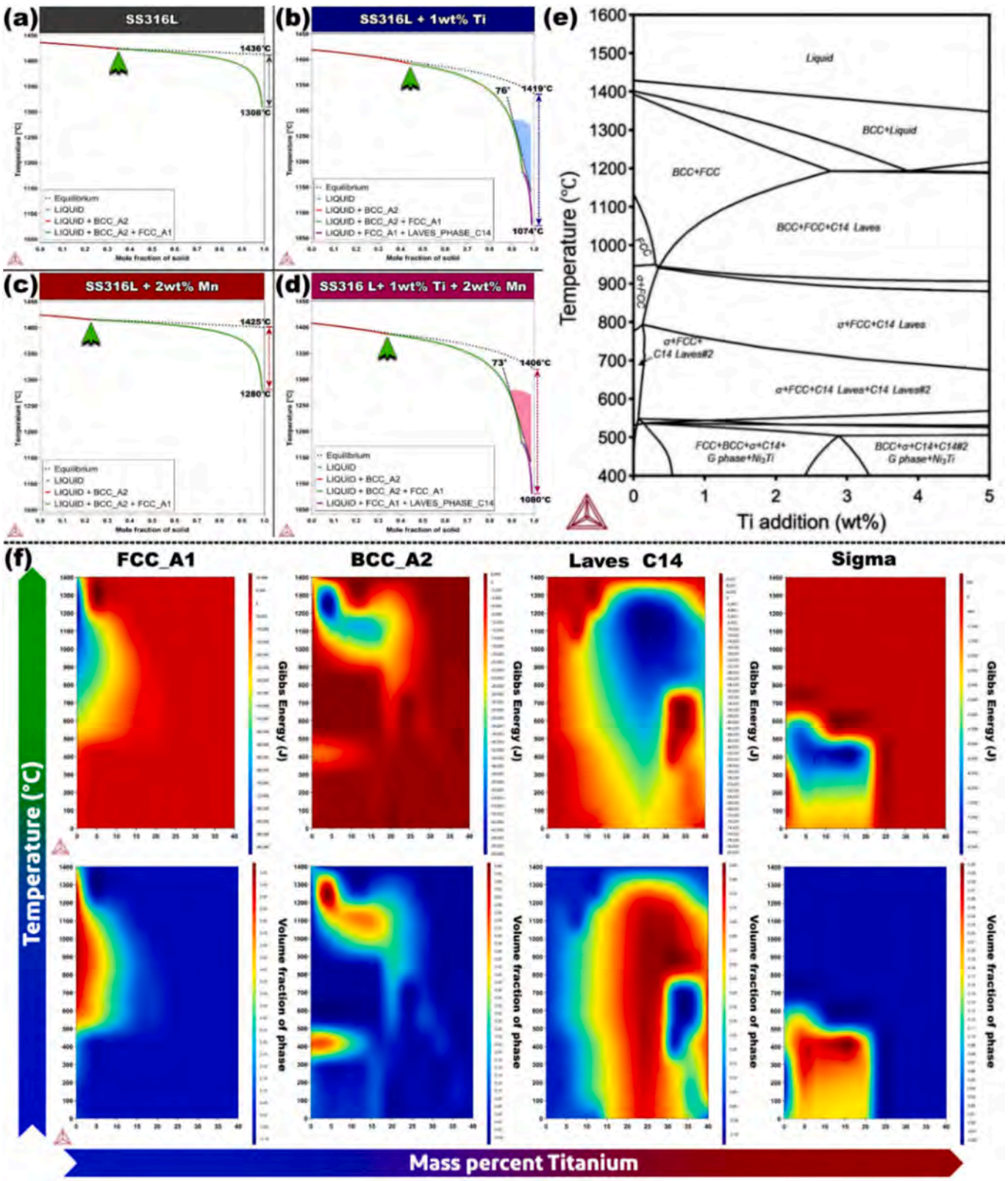

Fig. 1. Thermo-Calc simulation results for SS316L: (a) Scheil solidification curve, (b) with 1 wt% Ti, (c) with 2 wt% Mn, (d) with 1 wt% Ti and 2 wt% Mn, (e) pseudo-binary phase diagram of SS316L with 2 wt% Mn as a function of Ti addition, and (f) heat maps of ΔG_f (top) and phase volume fractions (bottom) as functions of temperature and Ti content.

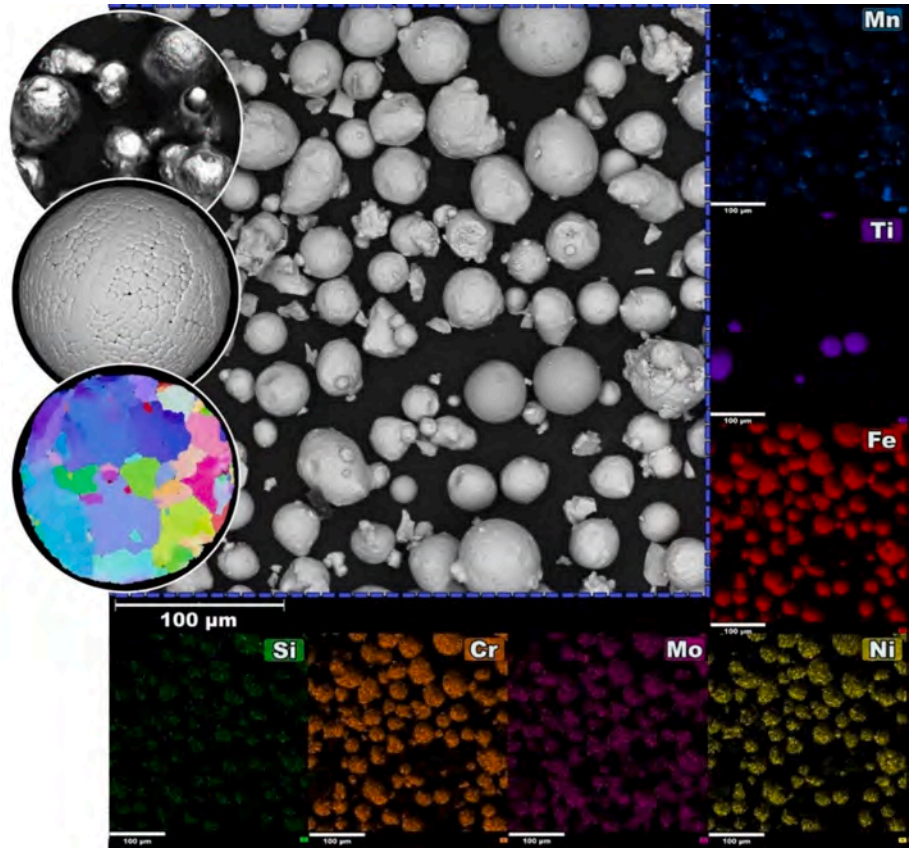

Fig. 2. SEM analysis of SS316L powder particles and blended powders used as feedstock.

annealing at 850 °C, 1050 °C, and 1250 °C for 1 h, followed by air cooling.

3.3. Mechanical examination

Two sample geometries were fabricated: (i) 10 × 10 × 10 mm^3 blocks for microstructural analysis and (ii) tensile bars (32 × 6 × 4 mm^3 gauge) conforming to ASTM E8. Specimens were sectioned from the build plate via wire electrical discharge machining (EDM), with tensile bars oriented perpendicular to the build direction. Quasi-static tensile tests were conducted at room temperature using a Zwick/Roell Z050 equipped with a laser extensometer, at a nominal strain rate of 2×10^{-3} s^{-1}. Each test was repeated thrice to obtain average values and standard deviations. Vickers microhardness measurements were performed using a VMHT system (0.1 kg load, 15 s dwell), with 20 linear indentations spaced 0.5 mm apart across the sample cross-section.

3.4. Microscopy characterizations

Metallographic specimens were mounted and polished using abrasive papers, followed by sequential polishing with diamond, alumina, and colloidal silica suspensions to a final finish of 0.05 µm. Chemical etching was performed using a mixed solution of 15 % HCl, 10 % HNO_3, and 1 % CH_3COOH for 10 s. Optical microscopy (OM) images were acquired using an Olympus DSX1000 digital microscope. For SEM analysis, non-etched samples were examined using JEOL JSM7001F and HITACHI SU-70 FEG-SEMs, both equipped with EBSD (EDAX-Hikari Plus) detectors. EBSD scans were conducted at 20 kV with a 0.1 µm step size, and data were processed using OIM Analysis™ and MTEX- MATLAB. TEM characterization was performed on FIB-milled foils using a dual-beam FEI Helios NanoLab and a JEOL JEM-2100F TEM operated at 200 kV. FIB-SEM imaging was carried out using a Thermo Scientific Helios 5 UC system, with surface illumination at 30 kV and 80 pA, and imaging via Ion Conversion and Electron (ICE) detector in SE mode. Prior to imaging, surfaces were etched with 30 kV ions at 21 nA for 30 s to expose microstructural features. Oxygen content was quantified using a LECO ONH836 analyzer.

3.5. Electrochemical measurements

Corrosion behavior was assessed via electrochemical testing using an Ivium-n-Stat potentiostat in a three-electrode cell configuration: the specimen as the working electrode, platinum wire as the counter electrode, and Ag/AgCl as the reference. Prior to testing, samples were polished to a mirror finish. A naturally aerated 3.5 wt% NaCl solution prepared with deionized water served as the electrolyte. All measurements were conducted at room temperature following a 30 min stabilization of the open circuit potential (OCP). Cyclic potentiodynamic polarization (CPP) was performed by sweeping the potential from - 0.2 V to + 1.0 V vs. OCP, reversing either at + 1.0 V or upon reaching 1 mA/cm^2. The scan rate was 10 mV/min with 1 mV increments. Corrosion potential (E_{corr}) and current density (I_{corr}) were extracted via Tafel extrapolation. Electrochemical impedance spectroscopy (EIS) was conducted by applying a 10 mV sinusoidal perturbation around the OCP. Impedance spectrum was recorded over a frequency range of 10^5 to 10^{-2} Hz, with 10 points per decade. Data were fitted using equivalent electrical circuits (EECs), where capacitance was modeled as a constant phase element (CPE), defined by the expression:

$$Z_{CPE} = \frac{1}{(j\omega)^n Q} \tag{2}$$

where "Q" is the CPE parameter having dimensions of s^n/Ω, $j = \sqrt{-1}$, $\omega = 2\pi f$ ("f" is the frequency) and "n" is a parameter that ranges between 0 and 1. All measurements were conducted in triplicate to ensure

reproducibility.

4. Results and discussions

4.1. Microstructural characterization

Fig. 3 presents OM and EBSD results for all LPBF-processed specimens: non-inoculated SS316L (Fig. 3(a-a3)), the as-built inoculated alloy (Fig. 3(b-b3)), and post-annealed states at 850 °C (Fig. 3(c-c3)), 1050 °C (Fig. 3(d-d3)), and 1250 °C (Fig. 3(e-e3)). Comparison of OM (Fig. 3(a, b)) and EBSD IPF maps (Fig. 3(a1, b1)) reveals that Ti addition alters grain morphology, producing ultrafine grains in enrichment zones and small columnar grains in Ti-depleted regions. The kernel average misorientation (KAM) in the austenitic matrix of the as-built inoculated alloy (Fig. 3(b2)) is notably higher than in the original SS316L (Fig. 3 (a2)), indicating elevated geometrically necessary dislocation (GND) density due to local strain and lattice distortion from inoculation-induced phases. Despite high KAM in Ti-rich zones, the overall grain orientation spread (GOS) remains low (Fig. 3(b3) vs Fig. 3(a3)), suggesting a deformation mechanism that accommodates strain via steep local orientation gradients without extensive lattice rotation. With an HCP structure, Laves phases deform primarily via synchroshear as a basal slip mechanism involving coordinated motion of atomic layers that generates stacking faults without lattice expansion [40]. This mechanism, active at elevated temperatures, facilitates slip on energetically unfavorable planes through synchronized dislocation movement, minimizing grain rotation and explaining the low GOS values [41,42]. High KAM surrounding Ti-enriched zones further supports localized strain accommodation via GND accumulation. Annealing at 850 °C (Fig. 3(c-c3)) reduces Ti-rich regions and diminishes high-KAM areas, indicating partial recovery. Concurrently, low-GOS grains expand around these zones, likely driven by recrystallization initiated in highly strained regions. As recrystallized grains are typically strain-free and structurally uniform, their growth around Laves phases results in extensive low-GOS domains. Annealing at 1050 °C and 1250 °C promotes dissolution of coarse intermetallic clusters and enhances grain refinement through diffusion-driven phase rearrangement (Fig. 3(d-d3, e-e3)). The observed reduction in KAM and expansion of low-GOS regions corroborate this transformation. However, the appearance of coarse equiaxed grains with minimal KAM and GOS at 1250 °C suggests a transition from recrystallization to grain growth. Further insights into phase evolution and grain refinement mechanisms during high-temperature annealing are explored in the following sections.

Fig. 4 highlights the evolution of recrystallized grain fractions near Ti-enriched zones. As shown in Fig. 4(a), the ultrafine-grained region primarily comprises highly deformed grains, consistent with the elevated KAM values in Fig. 3(b2). With increasing annealing temperature, the fraction of deformed grains progressively decreases (Fig. 4(b-d)). However, even at 1250 °C, full recovery is not achieved, as evidenced by persistent high local misorientation between coarse

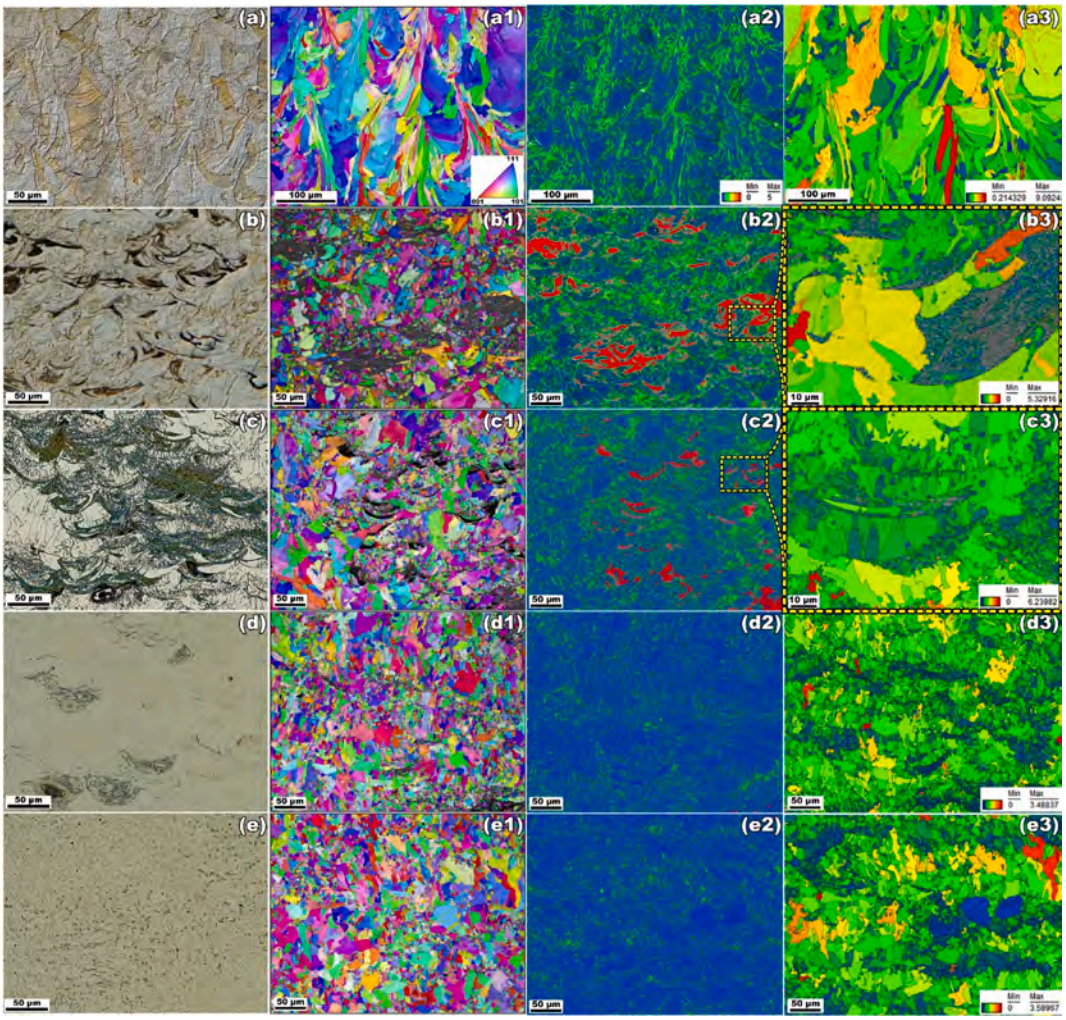

Fig. 3. OM, EBSD color maps, KAM and GOS maps of the non-reinforced SS316L (a-a3), reinforced sample in as-built state (b-b3), and after annealing at 850 °C (c-c3), 1050 °C (d-d3) and 1250 °C (e-e3) for 1 h.

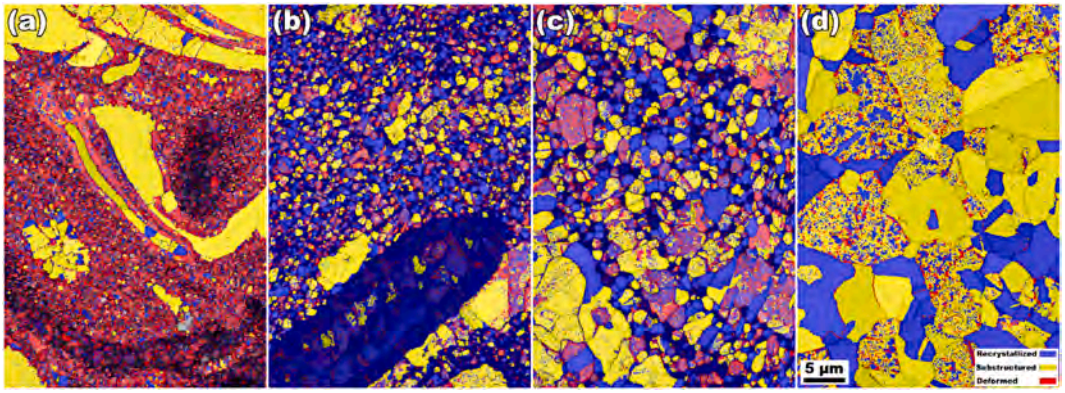

Fig. 4. EBSD recrystallization fraction map of TiMn inoculated specimens in as-built state (a), and after annealing at 850 °C (b), 1050 °C (c) and 1250 °C (d), respectively.

recrystallized grains in Fig. 3(e2). This suggests incomplete strain relaxation despite extensive thermal exposure.

Fig. 5 presents BSE-SEM images, IPF maps, and phase maps of the reinforced alloy in the as-built state and after annealing at various temperatures. In Fig. 5(a-a2), Ti incorporation within select melt pools produced ultrafine-grained zones featuring Laves phase cores encircled by ferritic grains, while adjacent Ti-depleted austenitic regions retained coarse grains. A compositional gradient is evident within the intermetallic complexes, transitioning from Laves to Laves-BCC (FeTi and ferrite), and ultimately to austenite. Annealing at 850 °C (Fig. 5(b-b2))

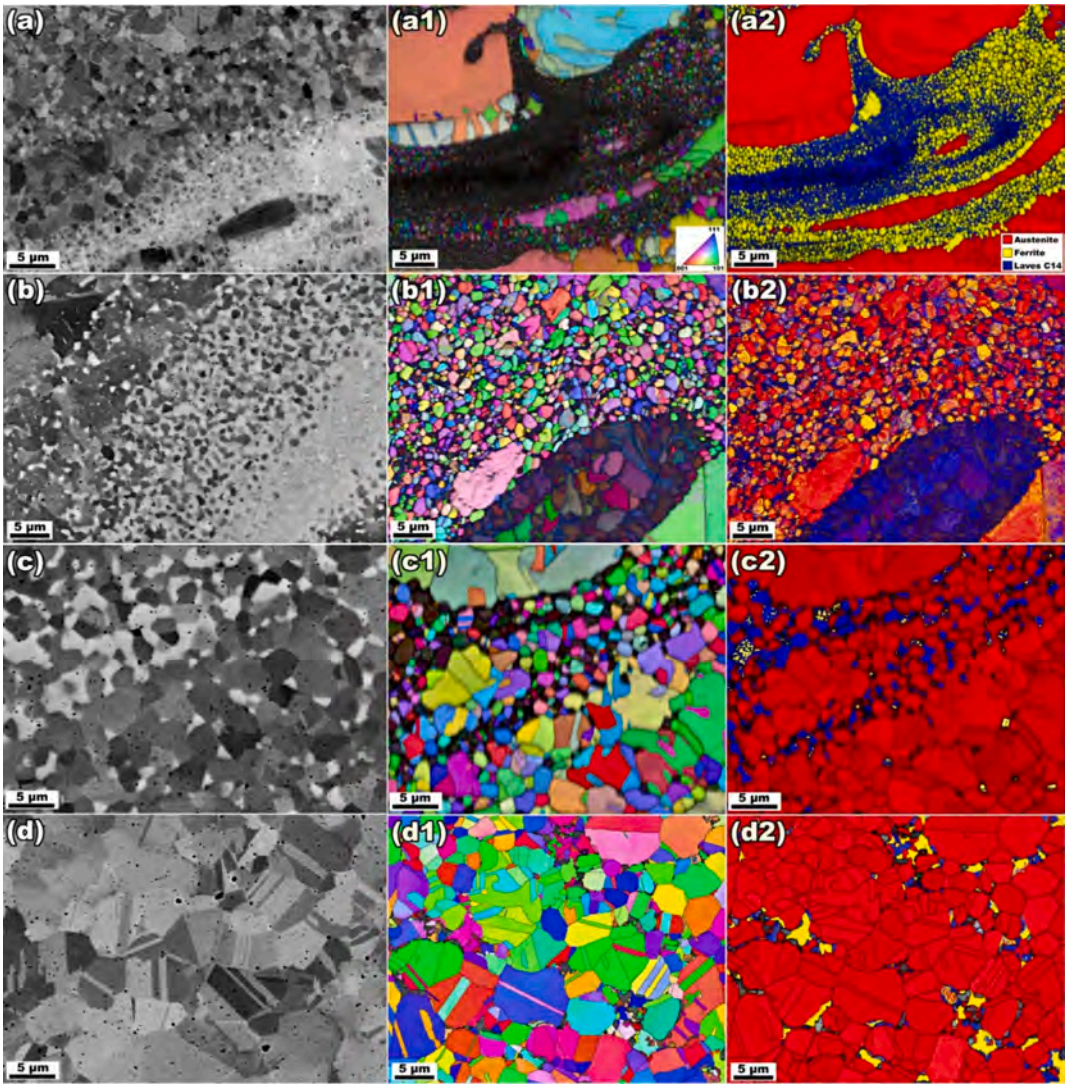

Fig. 5. BSE-SEM images, EBSD color maps, and EBSD phase maps of the as-built reinforced sample (a-a2), and after annealing at 850 °C (b-b2), 1050 °C (c-c2), and 1250 °C (d-d2), respectively.

led to partial dissociation of coarse intermetallics. Ti diffusion facilitated the formation of fine Laves phases around Ti-rich cores, predominantly along GBs and triple junctions, suggesting these sites act as preferential diffusion and nucleation pathways.

At elevated temperatures (Fig. 5(c-c2, d-d2)), enhanced solubility and diffusion kinetics promoted dissolution and redistribution of Laves clusters, accompanied by coarsening and stabilization of nearby austenitic grains. However, the dispersed Laves phases constrained grain growth, with the smallest austenitic grains observed in samples annealed at 850 °C and 1050 °C. Redistribution also promoted ferritic grain nucleation, consistent with Ti's ferrite-stabilizing role. The presence of thermal twins in austenitic grains (Fig. 5(c1, c2)) indicates recrystallization, though grain growth remained limited by surrounding Laves phases. Grain size analysis confirmed that Ti-Mn co-addition refined the average grain size from 38 μm in SS316L to 17 μm in the as-built alloy. Annealing at 850 °C had minimal impact on coarse intermetallics, while treatment at 1050 °C reduced grain size to 9.7 μm. A slight increase to 12.5 μm at 1250 °C reflects the grain-constraining effect of residual Laves phases.

The depletion of austenite-stabilizing elements near Laves phases increases the thermodynamic driving force for austenite-to-ferrite transformation. To elucidate phase evolution during annealing, TEM analysis was conducted on reinforced samples in the as-built state and after heat treatments at 850 °C and 1250 °C. EBSD band contrast images in Fig. 6 highlight the regions selected for TEM investigation, with detailed microstructural features presented in Figs. 7-11.

Fig. 7 presents TEM micrographs of the as-built reinforced sample, detailing phase evolution within a Ti-enriched intermetallic complex and its surrounding matrix. Fig. 7(a) offers an overview from the austenitic matrix at the base to the intermetallic core at the top. The Ti-rich center (Fig. 7(a1)) is dominated by FeTi with a BCC structure, confirmed by SAED pattern 1. During solidification, FeTi accommodated thermal shock via dislocation proliferation. As Ti concentration decreased outward, Fe_2Ti Laves phases formed, marked by a transition from dislocation-driven deformation to synchroshear mechanisms (Fig. 7(a2)), characteristic of HCP structures [40]. SAED pattern 4 identifies the outermost Laves layer, encased by ferritic grains (SAED pattern 3). Fig. 7(a4) reveals high GND densities in the adjacent austenitic matrix, accommodating thermal mismatch stresses and mitigating cracking during cooling. The EDS line-scan (Fig. 7(b)) confirms compositional gradients: Ti depletion and Fe/Cr enrichment transitioning from Laves to ferritic grains, followed by increased Fe and Ni with reduced Cr and Ti in the austenitic matrix. Comparison of SAED patterns 4 and 6 suggests the coexistence of multiple Laves variants with hexagonal symmetry but differing lattice parameters, consistent with deviations from stoichiometric Fe_2Ti [43,44]. TEM images (Fig. 7(a1, a5)) support GOS analysis (Fig. 3(b3)), linking synchroshear band formation and localized stress accommodation to high-GOS grains within Ti-enriched zones.

Fig. 8(a) shows TEM micrographs of an intermetallic complex (green box) and its surrounding region in the reinforced sample annealed at 850 °C for 1 h. The complex is encircled by ultrafine grains (<1 μm), and several regions were analyzed to elucidate the mechanisms driving grain refinement. Magnified views of the core (Fig. 8(a1, a2)) reveal pronounced dislocation accumulation in the innermost zone, with SAED1 confirming a superlattice BCC FeTi phase. These domains accommodated solidification-induced stresses via dislocation generation. Adjacent to the FeTi core, Fig. 8(a2) identifies Fe_2Ti Laves phases with HCP symmetry (SAED2), surrounded by additional Laves variants with distinct lattice parameters (SAED3, SAED4). Notably, dislocations within the BCC FeTi phase are uniformly dispersed, attributed to the high Peierls-Nabarro stress in BCC lattices, which impedes glide due to non-planar dislocation cores [41]. This restricts slip band formation and favors distributed strain accommodation. Further analysis of the surrounding ultrafine matrix revealed austenitic grains with thermal twins (SAED5) and Laves phases dispersed between them (SAED6).

To assess phase distribution and elemental diffusion after annealing at 850 °C, elemental mapping of intermetallic chunks and surrounding ultrafine grains was performed (Figs. 9-10). EDS maps and line-scan analysis (Fig. 9) reveal a compositional gradient from the austenitic matrix toward the intermetallic core, marked by Ti and Ni enrichment and depletion of Fe, Mn, Cr, and Mo. Minor Ti fluctuations are attributed to TiO nanoparticle formation. Point analysis (Fig. 9) confirms the BCC phase at the intermetallic core as (Fe,Ni)Ti, consistent with prior reports of Ni substituting Fe in FeTi during Ti deposition on SS316L [45]. Surrounding the core, distinct Laves phase cortexes form based on local solute availability. The outermost Laves layer, enriched in Cr and Fe and depleted in Ti, coincides with TiO nanoparticle formation. This susceptibility is linked to differences in crystal structure and diffusivity of oxygen and solute elements across the layers. These findings indicate that Ti-rich cores act as diffusion sources during annealing, driving Ti migration and TiO nanoparticle precipitation in adjacent phases.

Fig. 10 presents EDS elemental maps from the ultrafine-grained region surrounding Ti-rich intermetallics, alongside point analysis of austenitic grains adjacent to Laves phases and a line scan across the austenite-Laves interface. These results highlight the critical role of Laves phases in constraining austenitic grain growth (red in STEM), thereby promoting microstructural refinement. Compositional analysis

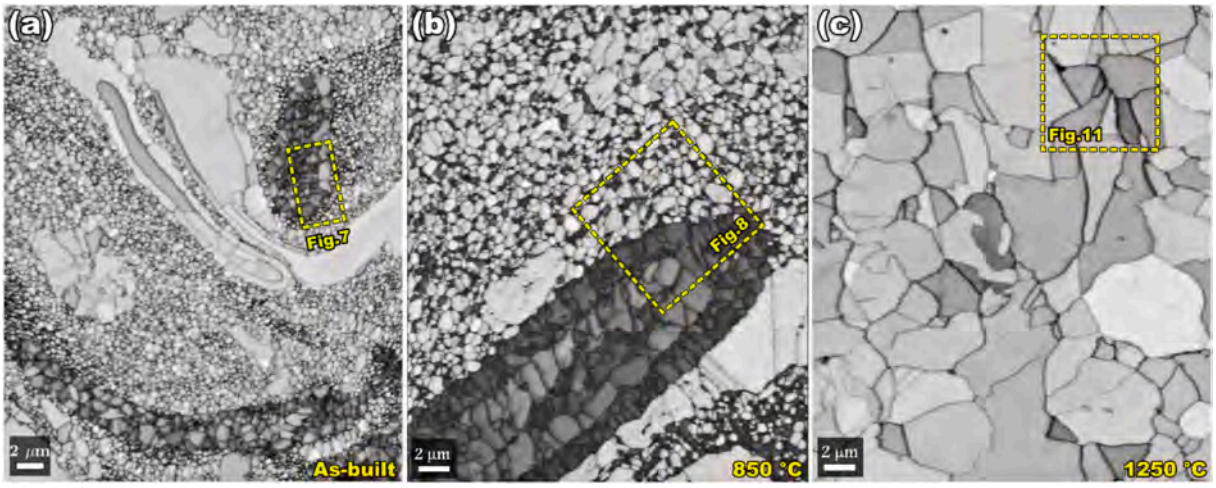

Fig. 6. EBSD band-contrast (BC) images showing the TEM analyzed zones in Figs. 7, 8 and 11 in the as-built reinforced sample (a) and after annealing at 850 °C (b), and 1250 °C (c), respectively.

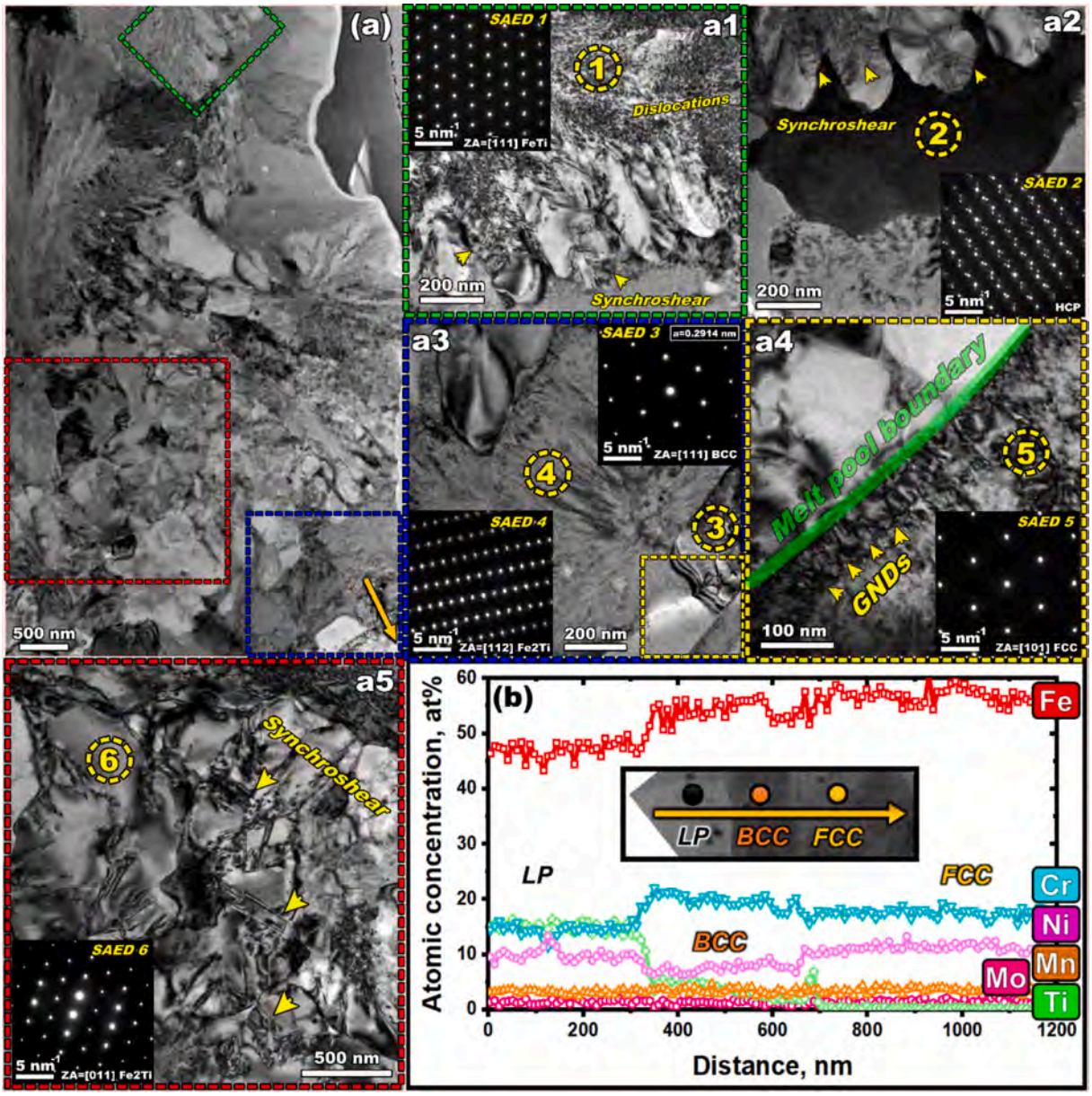

Fig. 7. TEM images (a1-a5) and corresponding SAED patterns and EDS line-scan at the interface of the intermetallic complex with surrounding ferritic grains and austenitic matrix (b) in the as-built reinforced sample.

reveals that Ti, Cr, and Mo dominate within Laves and ferritic phases, while austenitic grains are enriched in Fe and Ni.

Ti distribution within the ultrafine-grained regions does not exhibit preferential segregation of TiO nanoparticles at grain boundaries or triple junctions. However, prior studies on Ti additions in ferritic steels have shown that TiO nanoparticles act as effective grain refiners due to their minimal lattice mismatch with the ferritic matrix, which inhibits epitaxial grain growth. The extent of ferrite grain refinement has been reported to scale with Ti content [23,46]. In contrast, no orientation relationship (OR) has been identified between TiO and austenite that would enable similar refinement in austenitic regions. As shown in Fig. 5 (c), annealing at 1050 °C leads to coarsening of both austenitic grains and Laves phases within refined zones, accompanied by partial transformation of Laves into ferrite. Further annealing at 1250 °C enhances diffusion kinetics, promoting dissociation of Ti-rich clusters and broader Ti redistribution throughout the printed part. This, combined with Ti's ferrite-stabilizing effect, facilitates the formation of numerous ferritic grains, as illustrated in Fig. 5(d).

TEM analysis in Fig. 11 reveals the grain structure and phase arrangement after annealing at 1250 °C. SAED patterns in Fig. 11(a), along with EDS mapping and line-scan data, confirm the coexistence of recrystallized austenitic and ferritic grains. The magnified region in Fig. 11(a1) shows a light-contrast phase concentrated at grain boundaries and triple junctions. Further magnification (Fig. 11(a2)) identifies this phase as Laves (SAED 3), consistent with BSE-SEM observations. EDS point analysis (Fig. 11) indicates that Ti is relatively uniformly distributed across austenitic and ferritic grains following annealing. The key compositional distinction lies in elevated Fe and Ni concentrations in austenite, and slightly higher Mo and Cr levels in ferrite. Local depletion of Ni and Fe, coupled with Cr enrichment, enhances the thermodynamic driving force for austenite-to-ferrite transformation. Despite partial redistribution, Ti solubility in both phases remains limited. Consequently, excess Ti segregates to grain boundaries and triple junctions, where it precipitates as Laves phases. These regions serve as preferential diffusion pathways during annealing, facilitating Ti migration and subsequent Laves phase formation upon cooling [47,48].

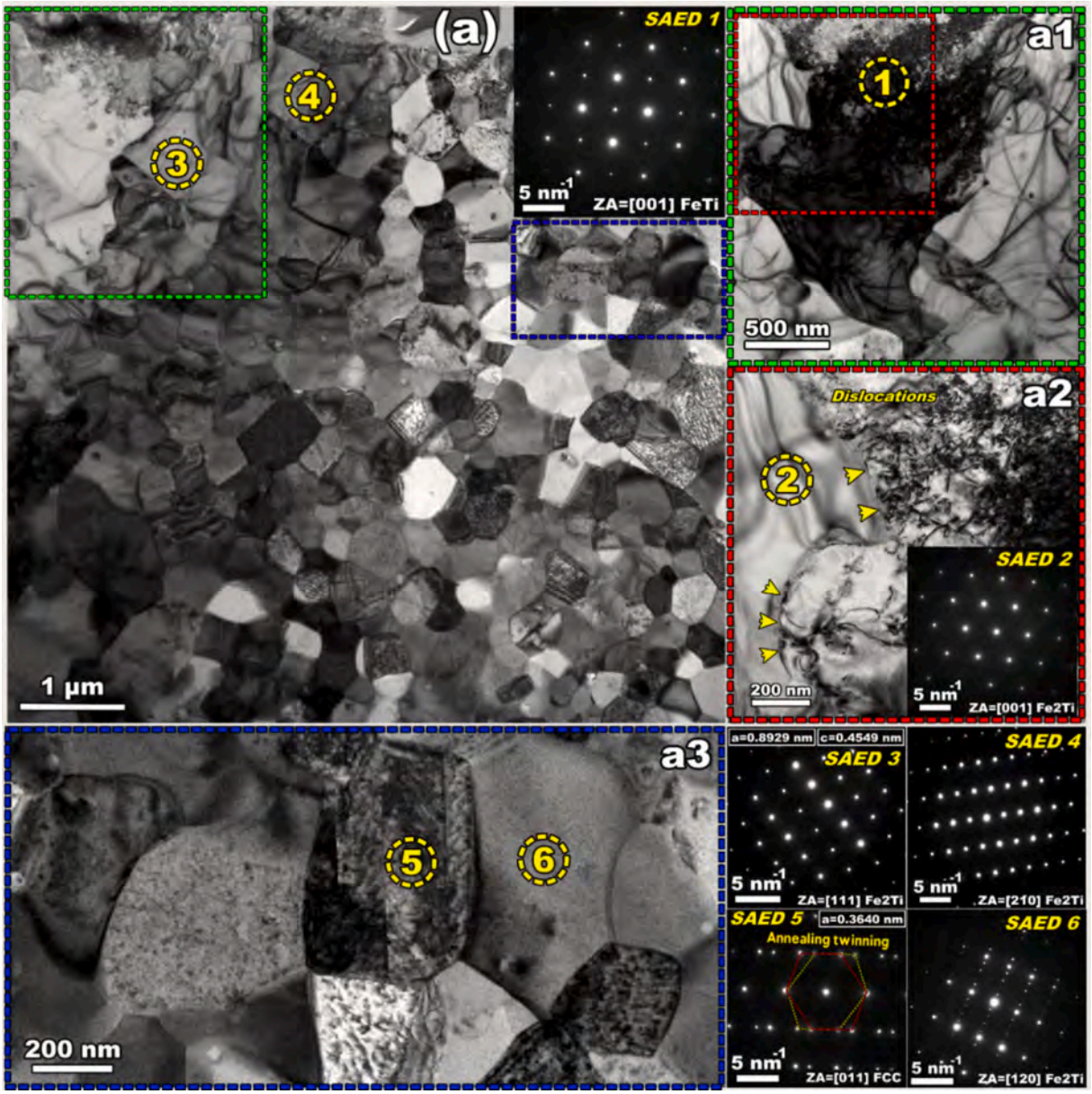

Fig. 8. TEM images (a-a3) and corresponding SAED patterns in the reinforced sample after annealing at 850 °C for 1 h.

Notably, Ti exhibits stronger segregation at austenite-ferrite interfaces than within the austenitic matrix, stabilizing Laves phases at these boundaries.

Upon annealing at 1250 °C, a portion of the inoculated Ti transformed into TiO particles, which were uniformly dispersed throughout the matrix. To elucidate the origin of these particles, the oxygen content of both the baseline SS316L and the reinforced alloy was quantified using LECO analysis. The results, summarized in Table 1, confirm increased oxygen uptake in the reinforced samples, supporting the formation of TiO precipitates during high-temperature exposure.

The incorporation of Ti into SS316L led to a measurable reduction in free oxygen content, as confirmed by LECO analysis. In additively manufactured SS316L, oxide inclusions such as rhodonite ($MnSiO_3$) and spinel ($MnCr_2O_4$) are commonly observed [49,50]. Prior studies have also shown that silicates like rhodonite and tridymite (SiO_2), with melting points of 1244 °C and 1703 °C respectively, undergo continuous dissolution and reformation during AM processing [51]. However, in Ti-reinforced samples, no Si-containing oxides were detected, suggesting either complete suppression or negligible formation. This implies that oxygen preferentially bonded with Ti, forming TiO particles rather than silicates. Although the formation enthalpy of TiO is higher than that of rhodonite and spinel under equilibrium conditions, the rapid solidification kinetics of PBF-AM favor TiO nucleation. These kinetics override thermodynamic preferences, leading to early TiO precipitation and limiting silicate formation [52–55]. Understanding the transformation behavior of TiO particles at different annealing temperatures is therefore critical to evaluating their role in microstructural evolution and alloy reinforcement. TEM analysis was conducted on samples annealed at 850 °C and 1250 °C to investigate TiO particle behavior. Fig. 12(a, b) show EDS maps of TiO particles located within Laves phases and austenitic grains, respectively. At 850 °C, coarse Ti-rich chunks act as Ti sources, dispersing TiO nanoparticles throughout the matrix, while Laves phases form in Ti-enriched zones between austenitic and ferritic grains. At 1250 °C, enhanced diffusion kinetics accelerate phase transformations, resulting in coarsening of grains, Laves phases, and TiO particles. Fig. 12(c) shows a TiO particle embedded within an FeTi grain located at the center of an unmelted region. Fig. 12(d, e) present the corresponding FFT, SAED, and IFFT analyses at the TiO-FeTi interface.

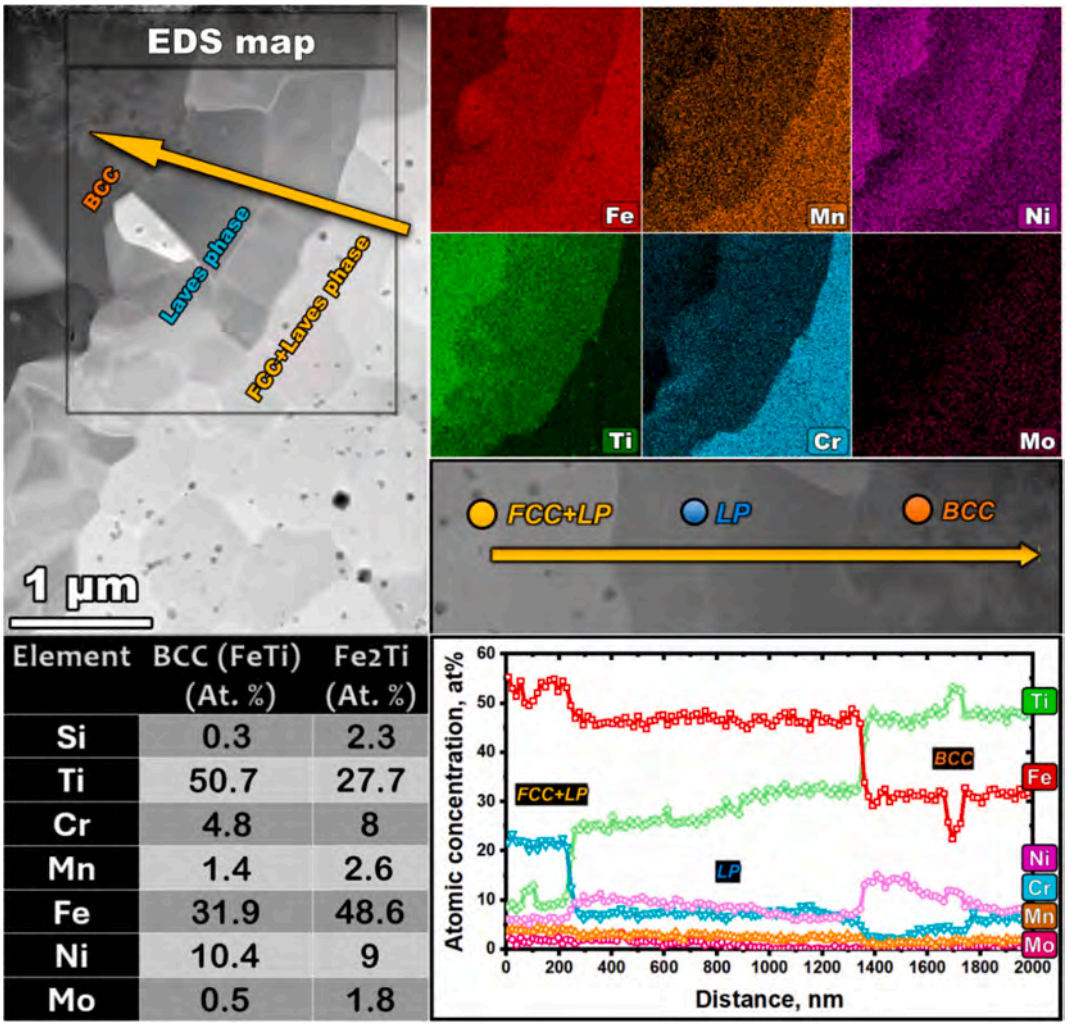

Fig. 9. STEM image and corresponding EDS point analysis and EDS line-scan at the interface of the intermetallic complex and steel matrix in the reinforced sample after annealing at 850 °C for 1 h.

The SAED patterns in Fig. 12(d), along with measured lattice spacings (0.213 nm for TiO and 0.259 nm for FeTi) indicate a lattice mismatch of ~ 18 %. This substantial misfit exceeds the ~ 5 % threshold typically required for effective heterogeneous nucleation, suggesting that TiO does not promote FeTi phase refinement. The presence of misfit dislocations surrounding the TiO particle further confirms the lack of a coherent interface with the matrix. In systems with minimal lattice mismatch, elastic strain is accommodated without dislocation formation. However, when the mismatch surpasses a critical value, strain accumulates at the interface, increasing the system's energy. To relieve this energy, misfit dislocations form, locally adjusting the atomic arrangement. The degree of coherency between the particle and matrix is thus governed by the interfacial mismatch. These dislocations typically emerge at elevated temperatures due to misfit-induced stresses and are absent around fully coherent inclusions [56,57]. Their presence is clearly visible in the TEM image (Fig. 12(c)) and the IFFT image (Fig. 12(e)).

Reported findings [41] have consistently shown that among Ti-based compounds added to ferritic steels (such as TiN and TiO) only TiO nanoparticles effectively serve as heterogeneous nucleation sites for ferrite, owing to their minimal lattice misfit. These nanoparticles also act as barriers to austenitic grain growth at elevated temperatures [41]. A comparison of the TiO dispersion map from TEM with the BSE and phase maps in Fig. 5, along with the band contrast images in Fig. 6, reveals that refined regions predominantly contain both TiO nanoparticles and ferritic grains. This observation aligns with the ferrite-stabilizing effect of Ti, as coarse intermetallic chunks are often encircled by ferritic grains, further refined by TiO inclusions. In contrast, areas distant from TiO agglomeration sites are characterized by coarser austenitic grains, particularly in the as-built condition.

4.2. Mechanical properties

In our previous study [39], we conducted an extensive comparison of the tensile properties of SS316L and the as-built reinforced samples, demonstrating that the co-addition of Ti and Mn improves tensile strength at the expense of ductility. TEM analysis (Fig. 7(a4)) reveals that rapid solidification promotes high-density GNDs around Ti-enriched zones. Although Ti-rich intermetallic complexes exhibit strong interfacial bonding with the matrix, the associated dislocations induce lattice distortions. These regions, characterized by synchroshear bands and brittle behavior, accommodate limited strain, resulting in elevated initial stress during deformation. Fig. 13(a, b) present engineering stress-strain, work-hardening, and true stress-strain curves for as-built and annealed samples (850 °C, 1050 °C, 1250 °C). Annealing at 850 °C reduces yield strength (YS) from 540 MPa to 470 MPa, while increasing ultimate tensile strength (UTS) from 645 MPa to 670 MPa and elongation from 12 % to 15 %. Although both as-built and annealed samples show a downward slope in Stage 2 of the work-hardening rate (Fig. 12(b)), the area under the $d\sigma/d\varepsilon$ vs. true strain curve increases after

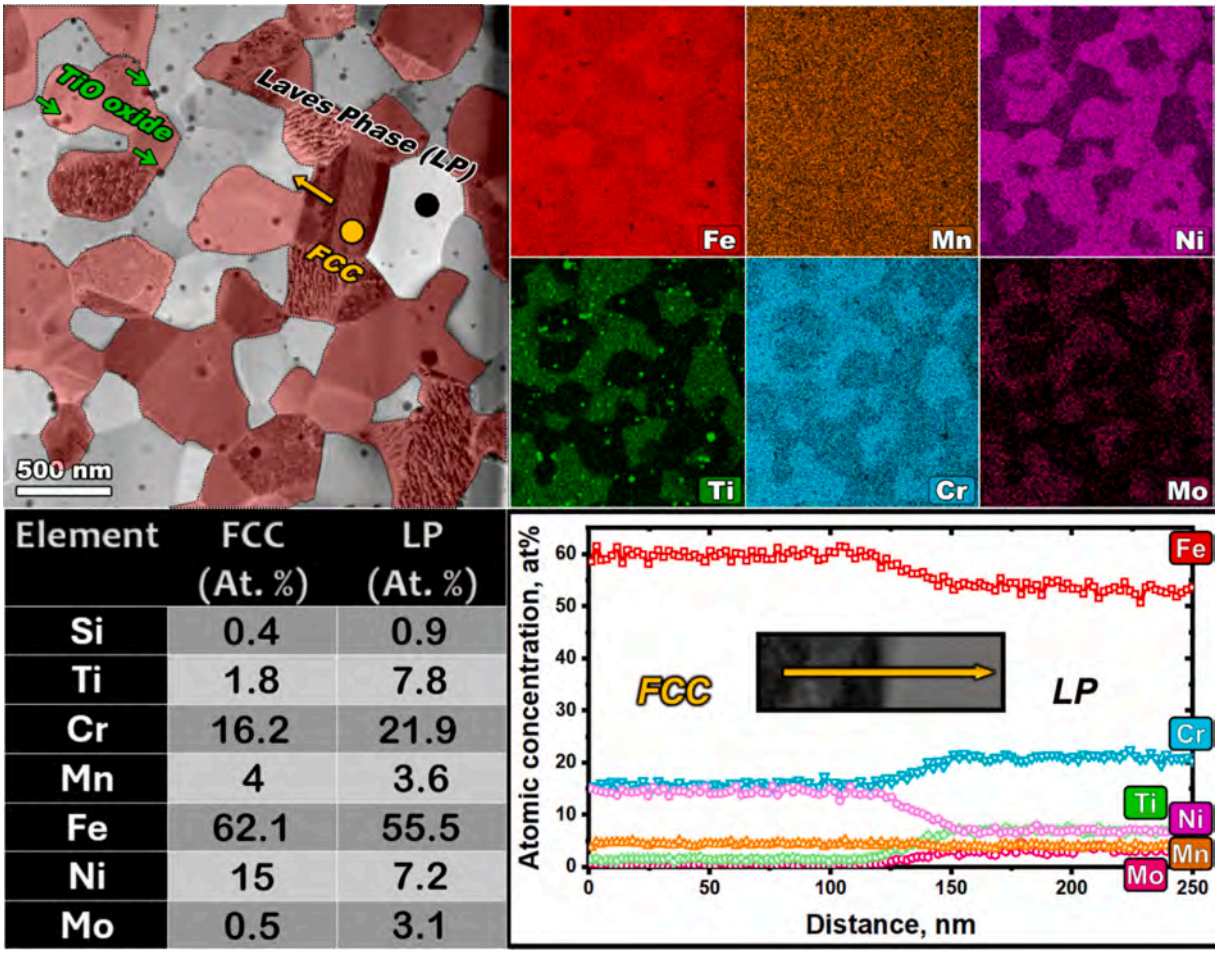

Fig. 10. STEM image and corresponding EDS point analysis and EDS line-scan at the fine-grained area surrounding the intermetallic chunks in the reinforced sample after annealing at 850 °C for 1 h.

annealing at 850 °C. Since this area reflects energy absorbed during plastic deformation, its smaller value in the as-built sample indicates reduced work-hardening capacity, limiting strain accommodation and accelerating necking.

The work-hardening rate evolves through three stages, marked by two inflection points: Stage 1 features a sharp decline from a high initial value; Stage 2 shows a slower descent as strain hardening and softening compete; Stage 3 exhibits a rapid drop, signaling the onset of necking and aligning with the UTS [58]. TEM analysis (Fig. 9) reveals that annealing at 850 °C partially dissolves Laves phases, redistributing finer precipitates throughout the matrix. This redistribution impedes dislocation motion and annihilation, thereby enhancing work hardening. The fine Laves phases serve as effective dislocation barriers, increasing storage capacity and delaying the onset of plastic instability. Annealing at 1050 °C significantly lowers yield strength (YS) while improving elongation, whereas annealing at 1250 °C results in a slight YS reduction but markedly enhances formability. The extended second stage of the work-hardening curve in the 1250 °C-annealed sample suggests improved strain hardening, likely driven by enhanced Ti diffusion and more uniform Laves phase dispersion. Additionally, finely distributed TiO particles and/or increased Ti content in the matrix further hinder dislocation motion and annihilation, delay entanglement, and facilitate greater strain accommodation prior to failure. Friction stress induced by alloying elements is also believed to suppress dislocation annihilation and contribute to elevated strain-hardening rates [59,60]. The hardness variation micrograph in Fig. 13(c) shows that the as-built reinforced sample exhibits a lower average hardness with a broader deviation range, reflecting the influence of dispersed coarse intermetallic chunks (up to 370 HV) within Ti-enriched zones embedded in the austenitic matrix, which typically exhibits ~ 250 HV in SS316L. Annealing at 850 °C narrows this deviation and raises the average hardness, attributed to the formation of fine Laves phases around coarse intermetallics and their nucleation at GBs. The enhanced tensile strength at this temperature may partly result from the GB pinning effect of these phases, although their presence could increase susceptibility to intergranular corrosion in aggressive environments. High-temperature annealing progressively removes microstructural features inherited from rapid solidification in AM, leading to a marked decrease in average hardness. Notably, annealing at 1250 °C further narrows the hardness variation, indicating a more uniform grain size and Ti-rich phase distribution. Despite the formation of fully equiaxed grains and a stress-relieved matrix, the average hardness of the annealed reinforced sample remains significantly higher than that of the as-built non-reinforced SS316L (215 vs. 180 HV).

Fig. 14 presents the 3D stereo micrograph and SEM images of the fracture surface, along with thru-thickness SEM views of tensile samples near their rupture zones. As shown in Fig. 14(a1), the initial yielding under tensile loading in the as-built reinforced sample occurred within the intermetallic chunks, particularly the Ti-enriched central phases. SEM analysis revealed multiple brittle phases on the fracture surface that fractured and collapsed, while the surrounding fine austenitic and ferritic grains resisted failure and formed ductile dimples. Notably, the intermetallic chunks exhibited strong interfacial adhesion to the matrix, such that failure was initiated only upon their yielding, not by debonding. The formation of microcracks introduced numerous stress localization sites, accelerating premature failure. Fig. 14(b1) shows that

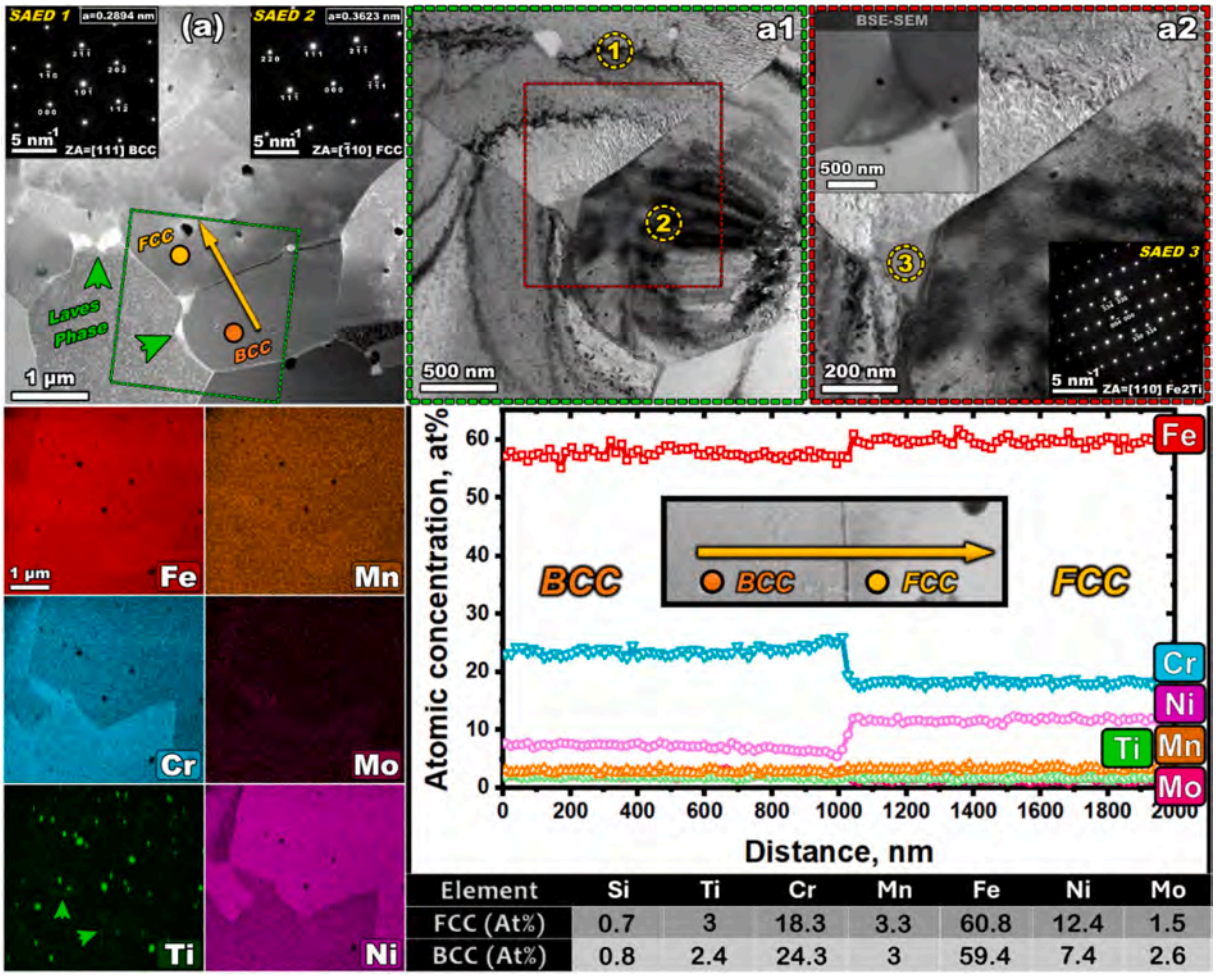

Element	Si	Ti	Cr	Mn	Fe	Ni	Mo
FCC (At%)	0.7	3	18.3	3.3	60.8	12.4	1.5
BCC (At%)	0.8	2.4	24.3	3	59.4	7.4	2.6

Fig. 11. TEM images (a-a3) and corresponding SAED patterns, EDS point analysis and EDS line-scan in the reinforced sample after annealing at 1250 °C for 1 h.

Table 1
The results of the LECO test.

Material	Oxygen (%)
Non-reinforced SS316L sample	0.0736 ± 0.00664
As-built reinforced SS316L sample	0.0588 ± 0.000709

annealing at 850 °C led to dissociation and more uniform nucleation of Laves phases at grain boundaries, distributing stress localization more evenly. Although the Laves phases were refined in size, they remained the dominant sites for crack initiation, with microcracks propagating into adjacent fine grains. Since fracture requires coalescence of these microcracks, failure was delayed. As illustrated in Fig. 14(b2), the fracture surface of the annealed sample at 850 °C features a mix of brittle cleavage facets and ductile dimples.

Fig. 14(c1) shows that annealing at 1050 °C, while partially restoring tensile strength, does not fully eliminate coarse brittle intermetallic phases, which continue to act as dominant fracture initiation sites. However, stress relief (evident from hardness measurements) enhances strain accommodation under tensile loading, delaying failure. This behavior is reflected in the formation of deep dimples, marked by brittle rupture at their bases and ductile elongation along coalescence walls.

A comparison of Fig. 14(a-c) with Fig. 14(d) reveals a pronounced increase in dimple size and overall deformation prior to failure following annealing at 1250 °C. As shown in Fig. 14(d1), even with a more uniform distribution of Laves phases at grain boundaries and triple junctions, these phases remain intrinsically brittle at room temperature. Consequently, they continue to serve as primary sites for yielding under mechanical stress. Fig. 14(d2) highlights their presence embedded within ductile dimples on the fracture surface of the 1250 °C-annealed sample.

4.3. Grain refinement and strengthening mechanisms

Disentangling the precise contribution of different factors to grain refinement and strengthening in such a complex, non-equilibrium system with evolving inhomogeneous compositions during annealing remains challenging. Nonetheless, correlating the microstructural evidence with the mechanical behavior presented in the earlier sections provides valuable insights into the underlying mechanisms. Characterization indicates that grain refinement in the as-built reinforced sample was predominantly localized within Ti-enriched clusters and their surrounding regions, while the growth of columnar austenitic grains was confined to the inter-cluster spaces. Given the comparable melting points of FeTi and Fe_2Ti Laves phases with SS316L [61,62] and the Scheil graphs in Fig. 1, the intermetallic phases did not serve as heterogeneous nucleation sites for SS316L. However, their formation in Ti-enriched regions restricted the growth of adjacent phases. Moreover, their ferrite-stabilizing character promoted the formation of fine ferritic grains around the Ti-rich clusters. As discussed earlier, during annealing the first recrystallized grains appeared near coarse phases, consistent with the activation of the particle-stimulated nucleation (PSN) mechanism. PSN occurs as recrystallization initiates within the highly strained zones surrounding large particles, with grain growth continuing until the stored strain is released [63]. The persistence of grain refinement,

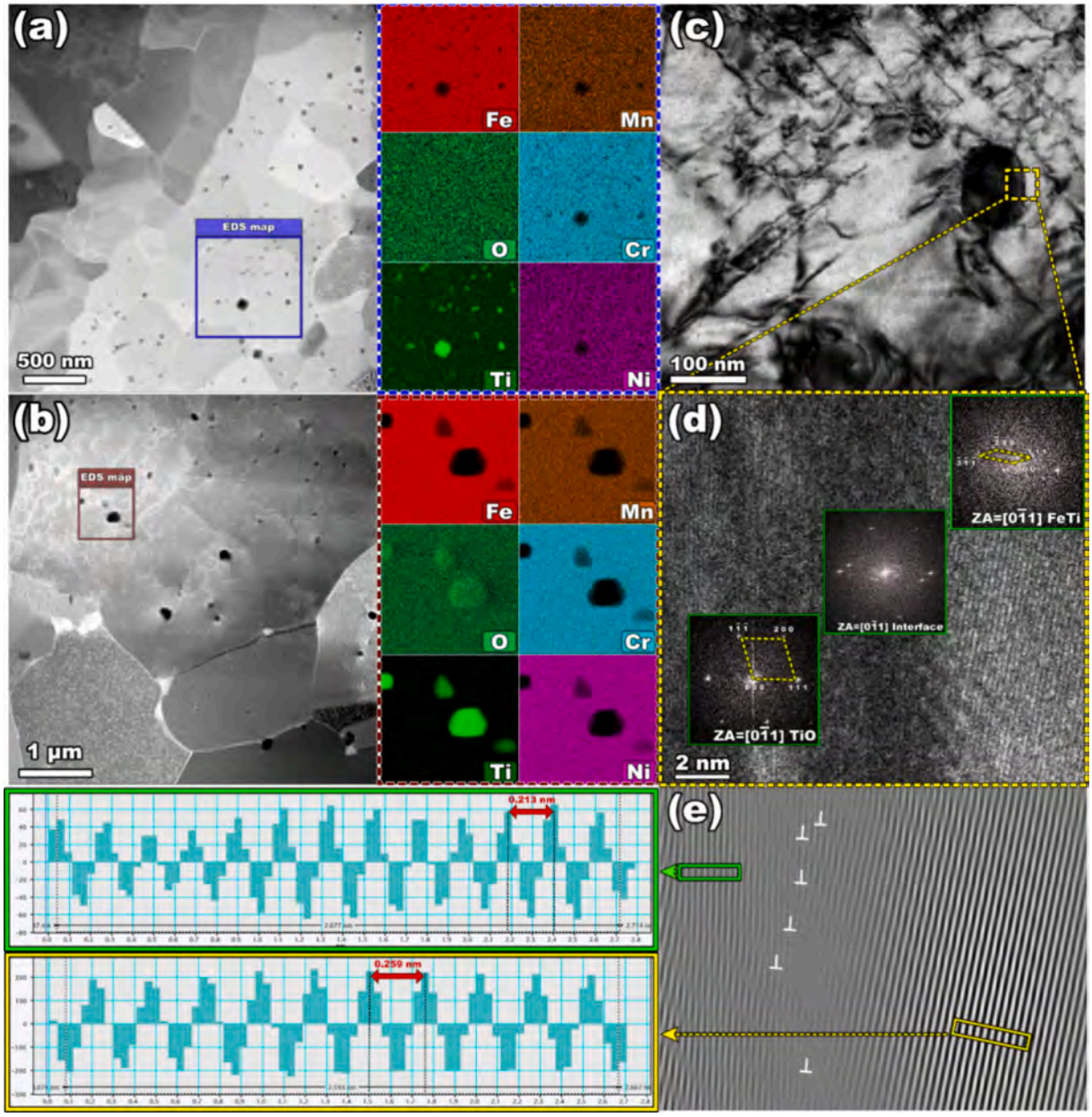

Fig. 12. TEM images and corresponding EDS maps of TiO particles in samples annealed at 850 °C (a) and 1250 °C (b) for 1 h. (c) Interface analysis of TiO particles and FeTi after annealing at 850 °C, with (d) FFT, (e) IFFT, and intensity profiles of atomic rows.

even at elevated annealing temperatures, is attributed to local Zener pinning exerted by dispersed TiO nanoparticles and fine Laves phases, which impede GB migration [64]. According to Zener pinning theory, the pinning pressure exerted by a random dispersion of spherical particles with radius r and volume fraction F is given by:

$$P_z = \frac{3Fv.\gamma}{2r} \tag{3}$$

here "P_z" is the pinning pressure (force/area) opposing boundary motion, "Fv" is the particle volume fraction, "r" is the particle radius, and "γ" is the GB energy (J·m^{-2}). Fan et al. [65] further argued that the mean matrix grain size scales linearly with the mean size of second-phase particles. Thus, a higher volume fraction of fine Laves phases and TiO nanoparticles enhances Zener pinning pressure on GBs, whereas their gradual coarsening diminishes this effect.

Multiple strengthening mechanisms contribute to the mechanical response of the reinforced SS316. However, due to the continuous variability and non-uniform distribution of phases within the matrix, these mechanisms are addressed qualitatively in the following discussion. Among them, Orowan strengthening, activated by TiO nanoparticles, represents one of the primary contributors [66]:

$$\sigma_{or} = \frac{0.4M}{\pi\sqrt{1-\upsilon}}.\frac{Gb}{\mathrm{L}}.ln\frac{\sqrt{\frac{2}{3}}.d_p}{b} \tag{4}$$

here

$$L = \sqrt{\frac{2}{3}}.d_p.\left(\sqrt{\frac{\pi}{4v_p}} - 1\right) \tag{5}$$

Here, "M" is the Taylor factor for 316L, "v" is Poisson's ratio, "G" is the shear modulus, "L" is the interparticle spacing, "b" is the Burgers vector, "d_p" denotes the average particle diameter (20-200 nm), and "v_p" represents the volume fraction of the particles. According to the Orowan mechanism, an increased particle volume fraction reduces interparticle

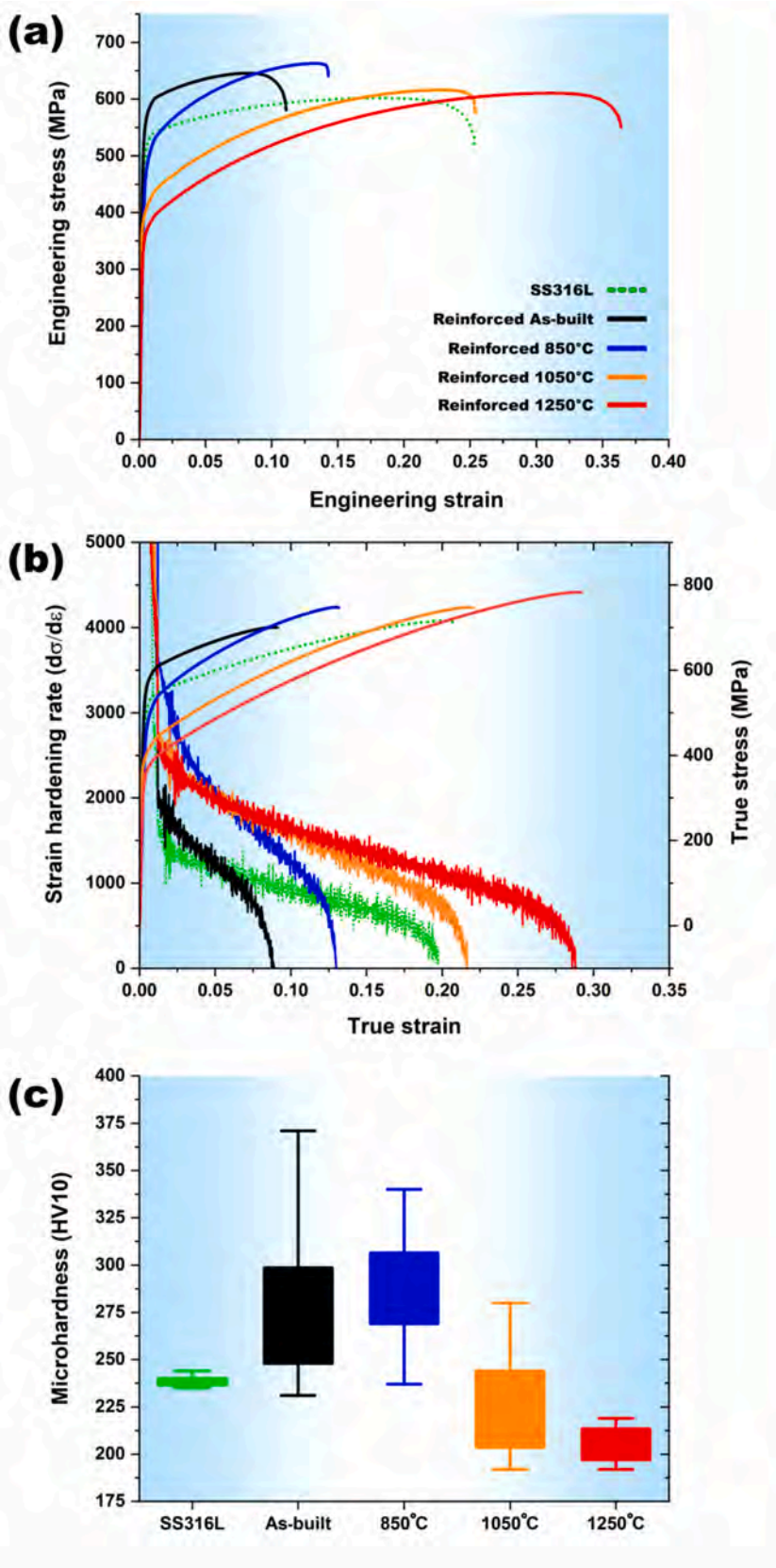

Fig. 13. Engineering stress-strain graphs (a), work-hardening rate and true stress vs true strain graphs (b) and Micro-hardness variation (c) in reinforced sample following annealing at different temperatures.

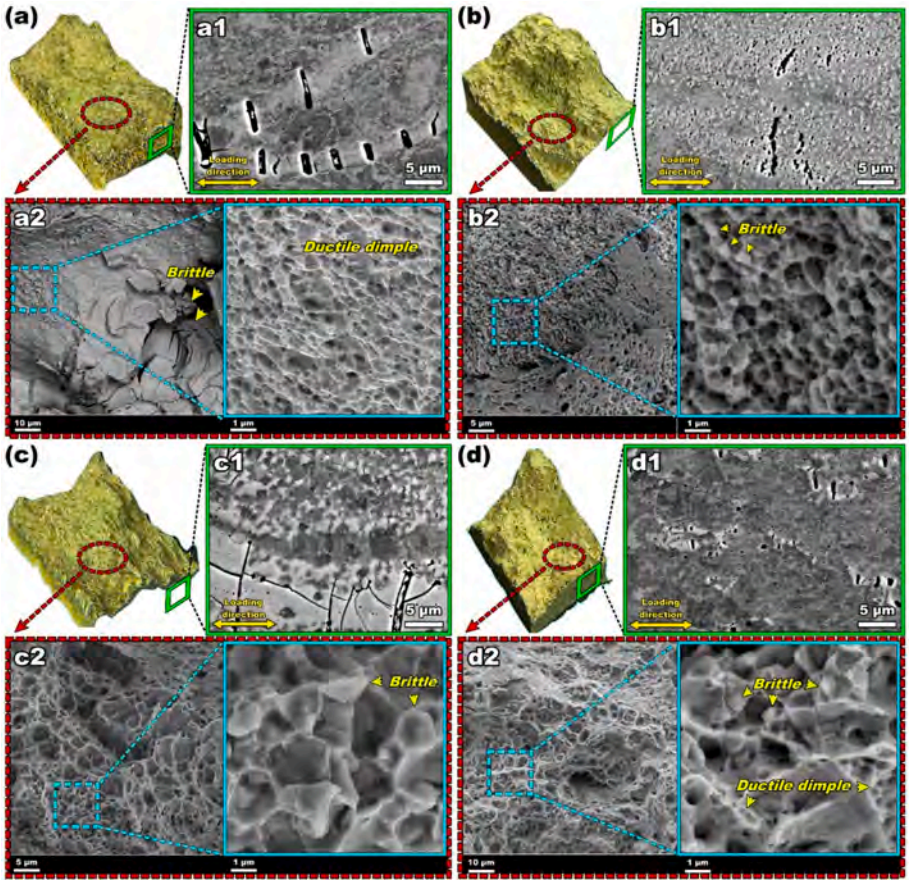

Fig. 14. Stereo-micrographs of the fracture surfaces (a-d) and corresponding SEM images taken from side section (a1-d1) and fracture surface (a2-d2) of the as-built reinforced sample (a-a2) and after annealing at 850 °C (b-b2), 1050 °C (c-c2) and 1250 °C (d-d2), respectively.

spacing, thereby enhancing Orowan stress (σ_{or}), whereas particle coarsening diminishes this effect.

Another strengthening contribution in the reinforced SS316L, particularly in the as-built condition, arises from the density of GNDs. Rapid solidification induces differential contraction between the austenitic matrix and intermetallic chunks, generating plastic strain incompatibility at their interfaces. The matrix accommodates this mismatch through GND formation. The strengthening contribution of GNDs to the yield stress (σ_y) can be expressed by the Taylor relation [67]:

$$\sigma_{GND} = \sqrt{3}\beta Gb.(\sqrt{\rho_{GND}}) \tag{6}$$

here, "β" is a geometric constant and "ρ_{GND}" represents the density of GNDs. During annealing, GND annihilation reduces their strengthening contribution. Given the strong interfacial bonding of Laves phases with the surrounding matrix and their predominantly brittle failure, load transfer strengthening between the matrix and reinforcement must also be considered. The yield strength increment due to the load transfer effect can be expressed as [68]:

$$\sigma_{LT} = \frac{1}{2}v_p\sigma_m \tag{7}$$

where "σ_m" is the strength of the SS316L alloy matrix. Due to the complex composition and the intertwined phases within the intermetallic chunks, precise estimation of their volume fraction was not feasible. In the reinforced SS316L, resistance to dislocation motion is largely governed by GBs, which impede glide due to misorientation between adjacent grains. Consequently, grain refinement increases the density of these barriers, enhancing the overall strength. This grain size-strength relationship is described by the Hall-Petch equation [69]:

$$\sigma_{HP} = \sigma_0 + kd^{-1/2} \tag{8}$$

Here, "σ_0" denotes the friction stress in the absence of GBs, "k" is the Hall-Petch constant representing the stress required to activate plastic flow at a GB, and "d" is the grain size. Annealing modifies the grain size contribution to strengthening by refining coarse columnar grains located between Ti-rich clusters while promoting slight coarsening of grains adjacent to intermetallic chunks. The room-temperature yield strength of the reinforced alloy after annealing at different temperatures can be estimated as the root mean square of the contributing strengthening mechanisms [66]:

$$\sigma_y = \sigma_{matrix} + \sqrt{{\sigma_{or}}^2 + {\sigma_{HP}}^2 + {\sigma_{GND}}^2 + {\sigma_{LT}}^2} \tag{9}$$

It should be noticed that contribution of the ferritic grains as well as precise volume fraction of the FeTi and Laves phases, were not considered, which may influence the presented equation.

Given the broad range of applications of SS316L due to its exceptional corrosion resistance, it is essential to investigate how the observed phase transformations influence the material's response in corrosive environments. Therefore, CPP and EIS measurements were conducted on the reinforced samples, and the vulnerable regions within these samples under exposure to aggressive environments were explored in the following.

4.4. Corrosion behavior

Significant phase transformations and variations in phase size and distribution were expected to markedly influence the electrochemical

behavior and corrosion kinetics of the alloy. The results from CPP measurements are presented in Fig. 15, and the computed E_{corr} and I_{corr} values are reported in Table 2. In the as-built reinforced sample, the E_{corr} shifted toward less noble, more negative values compared to SS316L, with further shifts observed at elevated annealing temperatures. These changes reflect alterations in phase distribution and are accompanied by corresponding variations in corrosion kinetics, as indicated by I_{corr}. The CPP curve of the as-built reinforced sample (exhibiting the lowest Icorr and thus the lowest corrosion rate) was the only one to display a passive region on the anodic branch, extending up to ~ 240 mV above E_{corr}. Our previous work has shown that high stored energy and a uniform distribution of fine surface grains promote the formation of a stable passive layer, enhancing adhesion and resistance to ion penetration [70]. This passive behavior typically appears as a plateau in the anodic branch, where current remains constant despite increasing overpotential. However, in this case, the anodic branch reveals metastable pitting, evidenced by multiple current spikes between −100 mV and + 200 mV vs Ag/AgCl (Fig. 15), indicating imperfect passivation [71]. Microstructurally, the as-built reinforced sample comprises Ti-rich Laves phases surrounded by fine ferritic grains within an austenitic matrix. While fine grains support passive layer formation, coarse intermetallic chunks remain highly susceptible to corrosion, correlating with the current peaks observed in the CPP curve. Upon annealing, dissociation and redistribution of Laves phases reduce these peaks, resulting in smoother polarization curves and diminished hysteresis between pitting and protection potentials. However, this transition also leads to stable pitting and a marked increase in current density and corrosion rate, with the 1250 °C-annealed sample exhibiting the highest degradation. The passive regions progressively shrink or vanish with increasing annealing temperature, limited to narrow overpotential ranges. All samples show hysteresis in the anodic branch, confirming imperfect passivation. Accelerated corrosion kinetics post-annealing arise from a combination of detrimental effects. Austenitic stainless steels rely on a Cr-rich (Cr_2O_3) passive layer for corrosion resistance, but annealing promotes Ti diffusion, ferrite formation, and local Cr depletion in the austenitic phase, increasing pitting susceptibility. Additionally, Ti segregation at grain boundaries and Laves phase formation at these sites heightens vulnerability to intergranular corrosion (IGC). The increased presence of TiO particles at higher annealing temperatures may further exacerbate corrosion, as their distinct electrochemical potential relative to the matrix makes them preferential sites for pitting. Grain growth and reduced stored energy during annealing also render these regions more susceptible to aggressive ion attacks.

To evaluate the effectiveness of the superficial oxide layer in promoting passivity, EIS measurements were performed on all samples, with results presented as Bode plots in Fig. 16 as Bode plots. At high frequencies (above 10^4 Hz), all samples exhibit resistive behavior, all samples exhibit resistive behavior, corresponding to the solution resistance. As frequency decreases, both the impedance modulus and phase angle increase, reflecting the response of the superficial oxide layer. In this intermediate frequency range, all samples display pseudo-capacitive behavior, with phase angles ranging from -80° to -60°, depending on the sample. At low frequencies (<1 Hz), the phase angle gradually declines, indicating a transition from capacitive to resistive-like behavior.

The impedance magnitude of the specimens closely follows the trend observed in the CPP curves. The as-built reinforced sample exhibits the highest impedance modulus, exceeding 10^5 Ω·cm^2, while annealing progressively reduces this value, consistent with the decline in corrosion resistance. As confirmed by potentiodynamic measurements, the as-built reinforced sample demonstrates superior corrosion resistance compared to SS316L, whereas elevated annealing temperatures accelerate corrosion rate. To further elucidate the corrosion mechanism, the impedance spectra were fitted using equivalent electrical circuit (EEC) models. Based on the spectral profiles, a single-time-constant circuit (Fig. 17(a)) was applied to the SS316L and as-built reinforced samples, while a two-time-constant circuit (Fig. 17(b)) was used for the annealed specimens. These models reflect distinct behaviors of the superficial oxide layer. In

Table 2
E_{corr} and I_{corr} values computed for all samples by means of Tafel extrapolation from CPP measurements.

	E_{corr} [mV vs Ag/AgCl]	I_{corr} [nA·cm^{-2}]
SS316L	−115 ± 6	138.0 ± 79.8
TiMn-As built	−146 ± 8	17.9 ± 5.2
TiMn-850 °C	−214 ± 30	77.9 ± 44.1
TiMn-1050 °C	−252 ± 67	145.2 ± 46.8
TiMn-1250 °C	−319 ± 41	587.1 ± 229.8

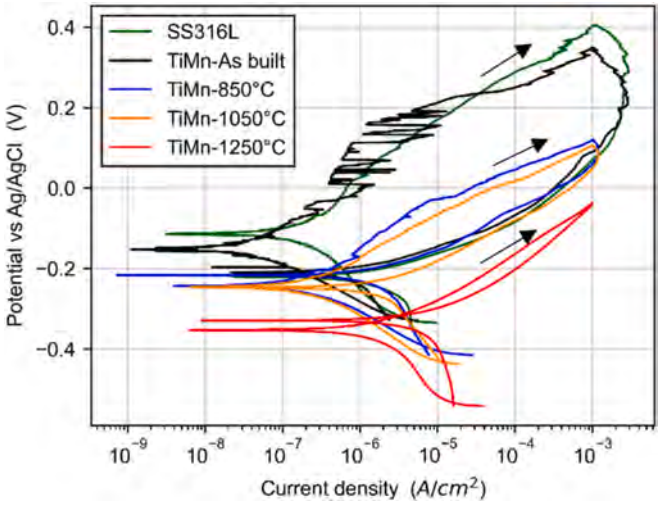

Fig. 15. CPP curves acquired on the samples in 3.5 wt% NaCl solution. The scan direction is indicated by black arrows.

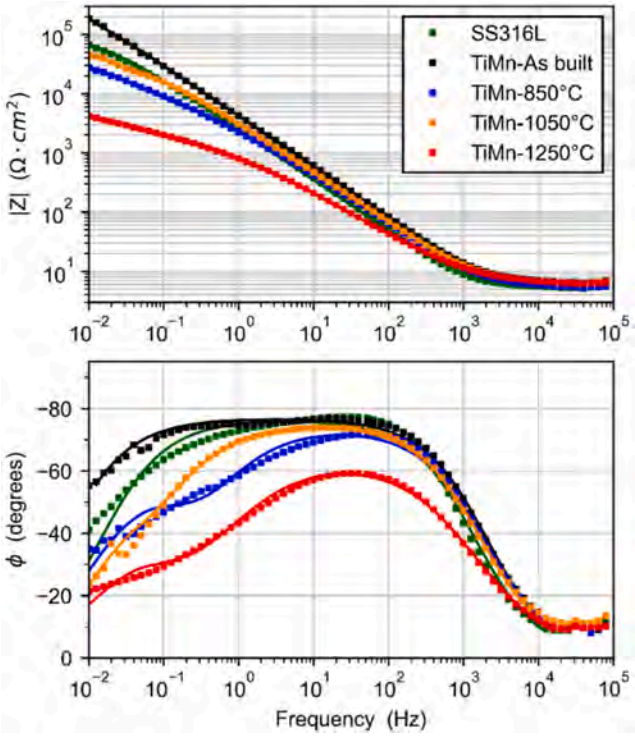

Fig. 16. Impedance spectra, reported as Bode plots, acquired on the samples in 3.5 wt% NaCl solution. The markers represent the experimental points, while the continuous line represents the EEC model.

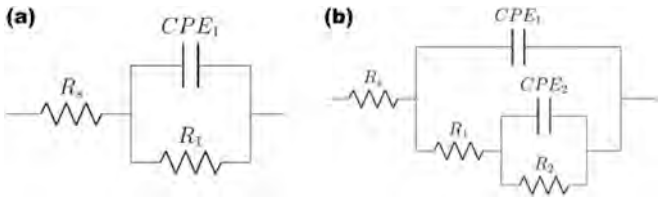

Fig. 17. (a) EEC used to model the impedance spectra acquired on SS316L and as-built reinforced samples; (b) EEC used to model impedance spectra acquired on annealed reinforced samples.

the single-time-constant configuration, the circuit comprises a solution resistance (R_s) in series with a parallel combination of R_1 and CPE_1, representing the oxide layer. For the annealed samples, the more heterogeneous nature of the oxide (arising from phase redistribution) necessitated a two-time-constant model. This circuit includes R_s, followed by a parallel CPE_2-R_2 pair in series with R_1 and CPE_1, capturing the layered and spatially varied oxide response. Fitting results are shown in Fig. 16 as continuous lines overlaid on the experimental data, and the extracted circuit parameters are listed in Table 3.

Analysis of the computed R_1 values, representing the superficial oxide layer, reveals a substantial decline from 2.52×10^5 Ω·cm^2 for the as-built reinforced sample to 3.36×10^3 Ω·cm^2 after annealing at 1250 °C. This reduction is accompanied by an increase in Q_1 and a decrease in n_1, indicating diminished protective behavior of the oxide layer. In contrast, the low-frequency parameters R_2 and Q_2 show no consistent trend with annealing temperature and contribute minimally to the overall impedance response, with R_2 consistently less than half of R_1. Their role in the EEC model is therefore attributed to surface heterogeneities arising from phase distribution, rather than representing distinct oxide layers. This interpretation is supported by SEM imaging following CPP measurements, which reveal the morphology of corrosion-induced degradation. As shown in Fig. 18(a), the as-built sample exhibits preferential attack on Ti-rich regions (red arrows), while the austenitic matrix remains largely unaffected. The increased prevalence of these domains in heat-treated samples correlates with accelerated corrosion kinetics and reduced impedance modulus. Additionally, oxide particles precipitated during annealing (yellow arrows in Fig. 18(b)) disrupt the continuity of the superficial oxide layer, serving as preferential sites for localized corrosion.

To identify corrosion-prone regions, FIB-SEM images of ion-etched surfaces were compared with SEM images of chemically etched samples (as described in the experimental section). As shown in Fig. 19(a, b), the as-built sample experienced pronounced corrosion in ultrafine regions, while the surrounding austenitic matrix remained largely unaffected. Post-annealing at 850 °C revealed refined grains and the emergence of numerous Laves phases at GBs, highlighted by yellow arrows in Fig. 19(c) and white contrast in Fig. 19(d). Following annealing at 1050 °C (Fig. 19(e, f)), transitional Laves phases at GBs were eliminated, and corrosion localized around fine Laves phases formed near initial agglomeration sites. These phases, being less noble than the austenitic matrix, intensified corrosion degradation, consistent with the observed decline in impedance modulus.

At 1250 °C (Fig. 19(g, h)), although the size of primary Laves phases (red arrows) was reduced, new interfacial Laves phases formed at GBs (yellow arrows), accompanied by a high density of TiO particles. The interface between ferritic grains, TiO particles, and the austenitic matrix introduces discontinuities in the superficial chromium oxide layer, rendering these regions highly susceptible to localized corrosion. The combined presence of Laves phases and TiO particles thus synergistically compromises the corrosion resistance of Ti-Mn co-inoculated SS316L.

5. Conclusions

In this study, Ti and Mn were co-inoculated into SS316L via LPBF in-situ alloying to promote grain refinement. Reinforced samples were subsequently annealed at 850 °C, 1050 °C, and 1250 °C for 1 h. Microstructural evolution was systematically characterized and correlated with mechanical performance and corrosion behavior. The key findings are summarized below:

- Thermodynamic simulations predicted the emergence of ferritic domains and Laves phases when local Ti concentrations exceeded 5-15 wt%. Co-addition of Mn was found to mitigate solidification cracking during printing.
- Local Ti enrichment led to heterogeneous grain refinement and the formation of FeTi and C14 Laves phase-rich zones, surrounded by fine ferritic grains within an austenitic matrix. Post-build annealing promoted dissociation of these complexes, transforming coarse primary Laves phases into fine interfacial layers at grain boundaries and triple junctions. Elevated annealing temperatures enhanced Ti diffusion, phase breakdown, and TiO nanoparticle dispersion, resulting in more uniform grain refinement and ferrite formation.
- Tensile testing revealed that failure in the as-built reinforced sample originated from coarse brittle Laves phases, despite intact interfaces with the matrix. Annealing at 850 °C modestly improved UTS and elongation to rupture (%El). Annealing at 1050 °C and 1250 °C significantly increased %El to 35 %, with only a slight reduction in UTS (from 650 MPa to 610 MPa). Despite phase refinement at 1250 °C, fracture still initiated at Laves phases, as evidenced by their brittle morphology within ductile dimples. Increasing annealing temperature narrowed hardness variation and reduced average hardness.
- Electrochemical analysis (CPP, EIS) and SEM imaging revealed that Ti-enriched zones in the as-built sample were highly prone to corrosion. Although the reinforced sample exhibited a lower average corrosion rate, annealing-induced phase transformations increased corrosion susceptibility, particularly at phase interfaces. Therefore, despite its grain-refining benefits, Ti addition to austenitic stainless steel compromises corrosion resistance and is not recommended.

CRediT authorship contribution statement

Mohammad Reza Jandaghi: Writing – original draft, Project administration, Methodology, Investigation, Formal analysis, Data curation, Conceptualization. **Hesam Pouraliakbar:** Formal analysis, Investigation, Conceptualization, Data curation, Validation, Resources, Writing – review & editing. **Sang Hun Shim:** Investigation, Formal analysis, Data curation, Resources, Writing – review & editing.

Table 3
EEC parameters computed for all samples (the reported values are the average of the 3 repetitions). See Fig. 16 for the meaning of the electrical parameters.

	Rs [Ω·cm^{-2}]	R1 [Ω·cm^{-2}]	CPE1		R2 [Ω·cm^{-2}]	CPE2	
			Q1 [s^n/(Ω·cm^2)]	n1		Q2 [s^n/(Ω·cm^2)]	n2
SS316L	5.5	1.24×10^5	8.5×10^{-5}	0.86			
TiMn-As built	6.1	2.52×10^5	6.5×10^{-5}	0.86			
TiMn-850 °C	5.8	2.81×10^4	1.6×10^{-4}	0.87	2.46×10^3	1.5×10^{-4}	0.84
TiMn-1050 °C	6.1	2.30×10^4	5.1×10^{-4}	0.89	1.02×10^4	1.4×10^{-4}	0.80
TiMn-1250 °C	5.9	3.36×10^3	1.6×10^{-3}	0.79	1.47×10^3	2.8×10^{-4}	0.71

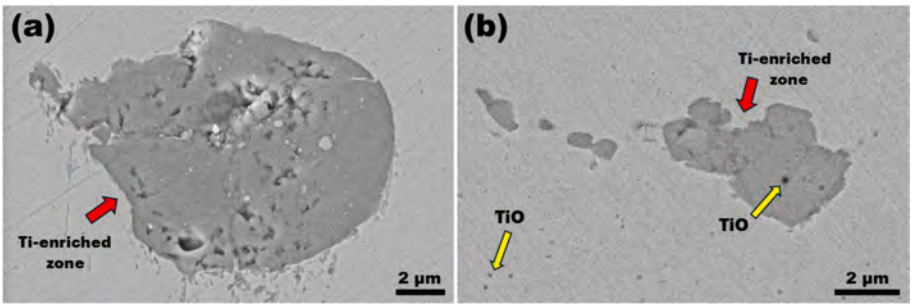

Fig. 18. SEM images of the reinforced sample in the as-built condition (a) and after annealing at 1250 °C (b), taken following the CPP tests. Preferential corrosion sites are indicated by colored arrows.

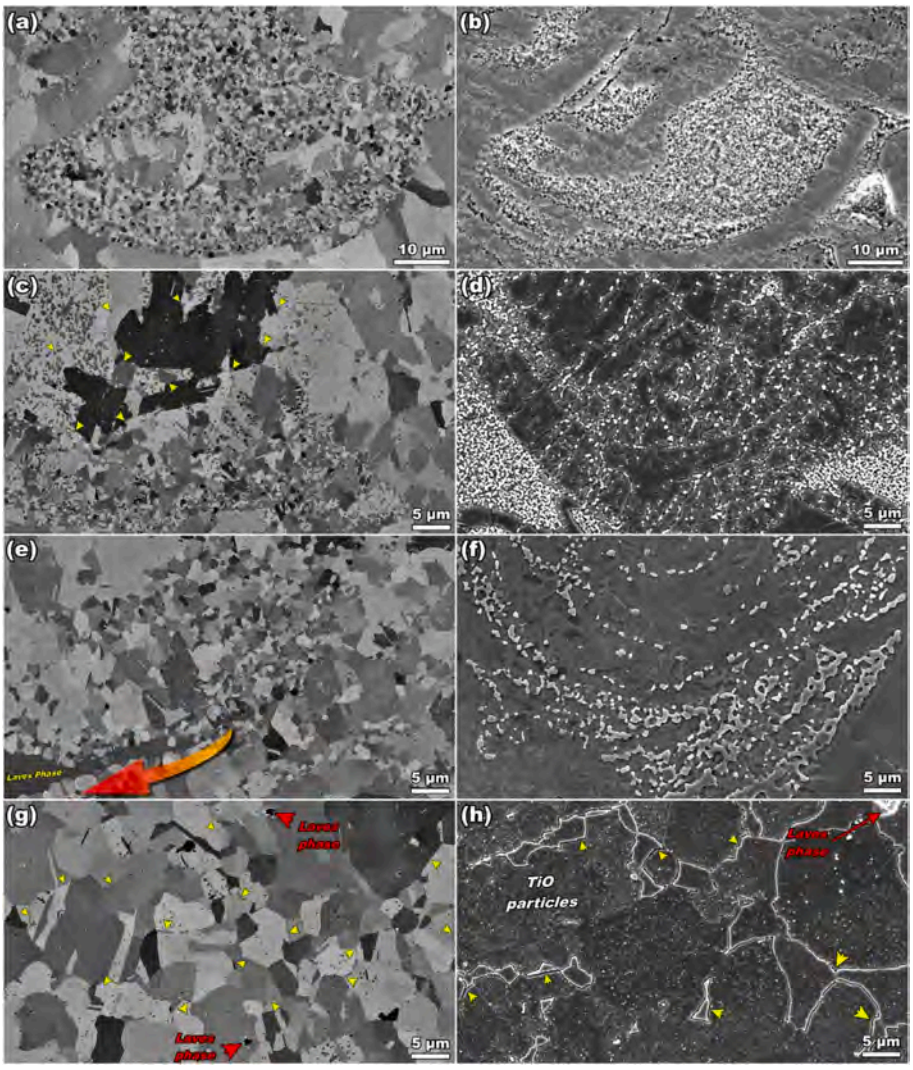

Fig. 19. FIB-SEM images (first column) before chemical etching and SE-SEM images (second column) after etching for the as-built reinforced sample (a, b) and after annealing at 850 °C (c, d), 1050 °C (e, f), and 1250 °C (g, h), respectively.

Leonardo Iannucci: Experimentation, Investigation, Formal analysis, Writing – original draft. **Prithwish Tarafder:** Investigation, Formal analysis, Writing – review & editing. **Justinas Palisaitis:** Investigation, Formal analysis, Writing – review & editing. **Sun Ig Hong:** Formal analysis, Resources, Writing – review & editing. **Suraj Y. Persaud:** Writing – review & editing, Formal analysis. **Vahid Fallah:** Formal analysis, Writing – review & editing. **Mattias Calmunger:** Formal analysis, Writing – review & editing. **Johan Moverare:** Formal analysis, Resources, Writing – review & editing.

Declaration of competing interest

The authors declare that they have no known competing financial interests or personal relationships that could have appeared to influence the work reported in this paper.

Acknowledgements

The authors gratefully acknowledge the Research Board of Chungnam National University (Republic of Korea), and Politecnico di Torino (Italy) for providing access to some of the facilities utilized in this study. Swedish Research Council and Swedish Foundation for Strategic Research acknowledged for access to ARTEMI, the Swedish National Infrastructure in Advanced Electron Microscopy (2021-00171 and RIF21-0026).

Data availability

No data was used for the research described in the article.

References

[1] T. Yang, S. Mazumder, Y. Jin, B. Squires, M. Sofield, M.V. Pantawane, N. B. Dahotre, A. Neogi, A review of diagnostics methodologies for metal additive manufacturing processes and products, Materials 14 (2021) 4929.
[2] H. Wei, J. Mazumder, T. DebRoy, Evolution of solidification texture during additive manufacturing, Sci. Rep. 5 (2015) 16446.
[3] S. Qu, J. Ding, J. Fu, M. Fu, B. Zhang, X. Song, High-precision laser powder bed fusion processing of pure copper, Addit. Manuf. 48 (2021) 102417.
[4] Z. Fan, C. Li, H. Yang, Z. Liu, Effects of TiC nanoparticle inoculation on the hot-tearing cracks and grain refinement of additively-manufactured AA2024 Al alloys, J. Mater. Res. Technol. (2022).
[5] Z. Wang, X. Wang, X. Chen, C. Qiu, Complete columnar-to-equiaxed transition and significant grain refinement in an aluminium alloy by adding Nb particles through laser powder bed fusion, Addit. Manuf. 51 (2022) 102615.
[6] X. Li, G. Li, M.-X. Zhang, Q. Zhu, Novel approach to additively manufacture high-strength Al alloys by laser powder bed fusion through addition of hybrid grain refiners, Addit. Manuf. 48 (2021) 102400.
[7] C. Burkhardt, M. Wendler, R. Lehnert, M. Hauser, P. Clausnitzer, O. Volkova, H. Biermann, A. Weidner, Fine-grained microstructure without texture obtained by electron beam powder bed fusion for AISI 304 L-based stainless steel, Addit. Manuf. 69 (2023) 103539.
[8] Y. Wang, Z. Liu, Y. Zhou, X. Yang, J. Tang, X. Liu, J. Li, G. Le, Microstructure and mechanical properties of TiN particles strengthened 316L steel prepared by laser melting deposition process, Mater. Sci. Eng. A 814 (2021) 141220.
[9] M.J. Bermingham, D.H. StJohn, J. Krynen, S. Tedman-Jones, M.S. Dargusch, Promoting the columnar to equiaxed transition and grain refinement of titanium alloys during additive manufacturing, Acta Mater. 168 (2019) 261–274.
[10] V.P. Narayana Samy, M. Schäfle, F. Brasche, U. Krupp, C. Haase, Understanding the mechanism of columnar-to-equiaxed transition and grain refinement in additively manufactured steel during laser powder bed fusion, Addit. Manuf. 73 (2023) 103702.
[11] P. Liu, Z. Wang, Y. Xiao, M.F. Horstemeyer, X. Cui, L. Chen, Insight into the mechanisms of columnar to equiaxed grain transition during metallic additive manufacturing, Addit. Manuf. 26 (2019) 22–29.
[12] H. Hizli, In-situ boron-induced grain refinement and its impact on the metallurgical and mechanical properties of Ti6Al4V alloy processed by laser powder bed fusion, University of Nottingham, 2024.
[13] C. Lu, Q. Jia, Z. Chen, Y. Cheng, Y. Song, X. Zhu, D. Gu, Solutes effect on grain structure and mechanical property evolution of Sc/Zr modified Al alloys fabricated by laser powder bed fusion, J. Alloy. Compd. 1011 (2025) 178444.
[14] L. Shoji Aota, P. Bajaj, H.R. Zschommler Sandim, E., Aimé Jägle, Laser powder-bed fusion as an alloy development tool: Parameter selection for in-situ alloying using elemental powders, Materials 13 (2020) 3922.
[15] X. Dan, C. Ren, Z. Song, S. Waqar, D. Zhang, M. Wang, Q. Liu, Y. Sun, X. Chen, W. Jiang, Exceptional strength and ductility in heterogeneous multi-gradient TiAl alloys through additive manufacturing, Acta Mater. 281 (2024) 120395.
[16] S.L. Sing, S. Huang, G.D. Goh, G.L. Goh, C.F. Tey, J.H.K. Tan, W.Y. Yeong, Emerging metallic systems for additive manufacturing: In-situ alloying and multi-metal processing in laser powder bed fusion, Prog. Mater Sci. 119 (2021) 100795.
[17] S. Wang, Z. Gao, G. Wu, X. Mao, Titanium microalloying of steel: a review of its effects on processing, microstructure and mechanical properties, Int. J. Miner. Metall. Mater. 29 (2022) 645–661.
[18] W. Zhai, W. Zhou, S.M.L. Nai, Grain refinement and strengthening of 316L stainless steel through addition of TiC nanoparticles and selective laser melting, Mater. Sci. Eng. A 832 (2022) 142460.
[19] W. Zhai, Z. Zhu, W. Zhou, S.M.L. Nai, J. Wei, Selective laser melting of dispersed TiC particles strengthened 316L stainless steel, Compos. B Eng. 199 (2020) 108291.
[20] J. Li, H. Qu, J. Bai, Grain boundary engineering during the laser powder bed fusion of TiC/316L stainless steel composites: New mechanism for forming TiC-induced special grain boundaries, Acta Mater. 226 (2022) 117605.
[21] A. Durga, N.H. Pettersson, S.B.A. Malladi, Z. Chen, S. Guo, L. Nyborg, G. Lindwall, Grain refinement in additively manufactured ferritic stainless steel by in situ inoculation using pre-alloyed powder, Scr. Mater. 194 (2021) 113690.
[22] H. Ikehata, D. Mayweg, E. Jägle, Grain refinement of Fe–Ti alloys fabricated by laser powder bed fusion, Mater. Des. 204 (2021) 109665.
[23] H. Ikehata, E. Jägle, Evaluation of microstructure and tensile properties of grain-refined, Ti-alloyed ferritic stainless steel fabricated by laser powder bed fusion, Mater. Sci. Eng. A 818 (2021) 141365.
[24] W. Zhai, W. Zhou, S.M.L. Nai, Grain refinement of 316L stainless steel through in-situ alloying with Ti in additive manufacturing, Mater. Sci. Eng. A 840 (2022) 142912.
[25] S.B. Han, Y.S. Lee, S.H. Park, H. Song, Ti-containing 316L stainless steels with excellent tensile properties fabricated by directed energy deposition additive manufacturing, Mater. Sci. Eng. A 862 (2023) 144414.
[26] D. Xu, W. Yang, M.P. Behera, S. Singamneni, M.A. Hodgson, P. Cao, Creating heterostructures via laser powder bed fusion using titanium and stainless steel mixtures, Mater. Sci. Eng. A 915 (2024) 147260.
[27] T. Zhang, Z. Huang, T. Yang, H. Kong, J. Luan, A. Wang, D. Wang, W. Kuo, Y. Wang, C.-T. Liu, In situ design of advanced titanium alloy with concentration modulations by additive manufacturing, Science 374 (2021) 478–482.
[28] C.-C. Hsieh, W. Wu, Overview of intermetallic sigma (σ) phase precipitation in stainless steels, International Scholarly Research Notices 2012 (2012) 732471.
[29] N. Nabiran, S. Weber, W. Theisen, Influence of Laves phase precipitation and coarsening on high-temperature strength of ferritic stainless steels, Steel Res. Int. 83 (2012) 758–765.
[30] I. Mohanty, S. Misra, S.K. Kar, P. Saha, Study of phase evolution, mechanical, and tribological behaviour of a novel β-phase strengthened Ti-alloy with Fe and Co alloying via a laser material deposition route, J. Alloy. Compd. 1007 (2024) 176469.
[31] H. Hyer, A. Mehta, K. Graydon, N. Kljestan, M. Knezevic, D. Weiss, B. McWilliams, K. Cho, Y. Sohn, High strength aluminum-cerium alloy processed by laser powder bed fusion, Addit. Manuf. 52 (2022) 102657.
[32] H. Pouraliakbar, M.R. Jandaghi, M. Gallerneault, A. Howells, J. Moverare, V. Fallah, Distinct phase evolution and deformation instability pattern in a Ce-modified Al-5Mg alloy, Mater Charact 227 (2025) 115265.
[33] S. Kou, A simple index for predicting the susceptibility to solidification cracking, Weld J. 94 (2015) 374–388.
[34] J. Liu, S. Kou, Crack susceptibility of binary aluminum alloys during solidification, Acta Mater. 110 (2016) 84–94.
[35] T. Soysal, A criterion to find crack-resistant aluminium alloys to avoid solidification cracking, Sci. Technol. Weld. Joining 26 (2021) 99–105.
[36] J. Liu, S. Kou, Effect of diffusion on susceptibility to cracking during solidification, Acta Mater. 100 (2015) 359–368.
[37] T. Soysal, Effect of solidification models on predicting susceptibility of carbon steels to solidification cracking, Weld. World 65 (2021) 1943–1954.
[38] C. Lee, Y. Lee, C. Lee, S. Hong, Precipitation behavior of the sigma phase with Ni and Mn content variations in superaustenitic stainless steel weld metal, Mater Charact 144 (2018) 148–154.
[39] M.R. Jandaghi, H. Pouraliakbar, S.H. Shim, V. Fallah, S.I. Hong, M. Pavese, In-situ alloying of stainless steel 316L by co-inoculation of Ti and Mn using LPBF additive manufacturing: Microstructural evolution and mechanical properties, Mater. Sci. Eng. A 857 (2022) 144114.
[40] Z. Xie, D. Chauraud, A. Atila, E. Bitzek, S. Korte-Kerzel, J. Guénolé, Unveiling the mechanisms of motion of synchro-Shockley dislocations in Laves phases, Phys. Rev. Mater. 7 (2023) 053605.
[41] J. Guénolé, F.-Z. Mouhib, L. Huber, B. Grabowski, S. Korte-Kerzel, Basal slip in Laves phases: the synchroshear dislocation, Scr. Mater. 166 (2019) 134–138.
[42] F. Stein, A. Leineweber, Laves phases: a review of their functional and structural applications and an improved fundamental understanding of stability and properties, J. Mater. Sci. 56 (2021) 5321–5427.
[43] S. Zhou, Y. Xu, B. Liao, Y. Sun, X. Dai, H. Pan, In-situ synthesis of Ti-Fe-based alloys prepared by the combination of mechanical alloying and laser melting deposition: Microstructure and corrosion resistance, J. Alloy. Compd. 768 (2018) 697–706.
[44] D. Boukhvalov, Y.N. Gornostyrev, M. Katsnelson, Uncommon clustering in dilute Ti-Fe alloys, Journal of Physics: Materials 3 (2020) 025007.
[45] J.-M. Auger, D. Cotton, C. Nouveau, A. Besnard, F. Bernard, M.-R. Ardigo-Besnard, J.-P. Monchoux, R. Cours, C. Marcelot, Comparison of thermal diffusion and interfacial reactions for bulk and sputtered titanium on 316L stainless steel, Mater. Chem. Phys. 306 (2023) 128013.
[46] X. Gan, Q. Yuan, G. Zhao, H. Ma, W. Liang, Z. Xue, W. Qiao, G. Xu, Quantitative analysis of microstructures and strength of Nb-Ti microalloyed steel with different Ti additions, Metall. Mater. Trans. A 51 (2020) 2084–2096.
[47] B. Straumal, O. Kogtenkova, P. Zięba, Wetting transition of grain-boundary triple junctions, Acta Mater. 56 (2008) 925–933.
[48] M.R. Jandaghi, H. Pouraliakbar, S.I. Hong, M. Pavese, Grain boundary transition associated intergranular failure analysis at TMAZ/SZ interface of dissimilar AA7475-AA2198 joints by friction stir welding, Mater. Lett. 280 (2020) 128557.
[49] M.R. Jandaghi, J. Moverare, Exploring the efficiency of powder reusing as a sustainable approach for powder bed additive manufacturing of 316L stainless steel, Mater. Des. 244 (2024) 113222.
[50] F. Yan, W. Xiong, E. Faierson, G.B. Olson, Characterization of nano-scale oxides in austenitic stainless steel processed by powder bed fusion, Scr. Mater. 155 (2018) 104–108.
[51] M.R. Jandaghi, A. Saboori, L. Iuliano, M. Pavese, On the effect of rapid annealing on the microstructure and mechanical behavior of additively manufactured stainless steel by Laser Powder Bed Fusion, Mater. Sci. Eng. A 142109 (2021).
[52] N. Derimow, N. Hrabe, Oxidation in reused powder bed fusion additive manufacturing Ti-6Al-4V feedstock: a brief review, JOM 73 (2021) 3618–3638.
[53] C. Lu, R. Zhang, X. Wei, M. Xiao, Y. Yin, Y. Qu, H. Li, P. Liu, X. Qiu, T. Guo, An investigation on the oxidation behavior of spatters generated during the laser powder bed fusion of 316L stainless steel, Appl. Surf. Sci. 586 (2022) 152796.

[54] M. Fontes, J. Capocchi, J. Acquadro, Study on Ti-SiO2 Reaction-Thermodynamic Approach, MRS Online Proceedings Library (OPL) 402 (1995) 27.
[55] S. Chandra-Ambhorn, T. Thublaor, C. Pascal, CHAPTER 1 Thermodynamics and Kinetics of the High Temperature Oxidation of Stainless Steels, Solid State Phenom. 300 (2020) 1–24.
[56] H. Long, H. Wei, Y. Liu, S. Mao, J. Zhang, S. Xiang, Y. Chen, W. Gui, Q. Li, Z. Zhang, X. Han, Effect of lattice misfit on the evolution of the dislocation structure in Ni-based single crystal superalloys during thermal exposure, Acta Mater. 120 (2016) 95–107.
[57] Y.N. Gornostyrev, M. Katsnelson, Misfit stabilized embedded nanoparticles in metallic alloys, PCCP 17 (2015) 27249–27257.
[58] J. Hu, D. Zhang, Z. Hu, S. Wang, L. Xiao, B. Gao, D. Yin, H. Zhou, Y. Zhao, Improving the uniform elongation of ultrafine-grained pure titanium through judicious allocation of work hardening, J. Mater. Process. Technol. 330 (2024) 118484.
[59] S.I. Hong, C. Laird, Mechanisms of slip mode modification in FCC solid solutions, Acta Metall. Mater. 38 (1990) 1581–1594.
[60] S.I. Hong, Criteria for predicting twin-induced plasticity in solid solution copper alloys, Mater. Sci. Eng. A 711 (2018) 492–497.
[61] T. Sugiura, S. Ishikawa, T. Matsuo, M. Takeyama, Phase equilibria between γ-Fe (A1) and Fe2Ti laves (C14) phases and microstructure in Fe-Ti-Ni ternary system at elevated temperatures, Trans Tech Publ, Mater. Sci. Forum, 2007, pp. 435–438.
[62] B. Hong, W. Jiang, L. Li-bin, L. Hua-shan, J. Zhan-peng, Thermodynamic re-assessment of Fe-Ti binary system, Trans. Nonferrous Met. Soc. Chin. 22 (2012) 2204–2211.
[63] M.S.J. Hashmi, Comprehensive materials processing, Newnes, 2014.
[64] S. Manna, H. Chan, A. Ghosh, T. Chakrabarti, S.K. Sankaranarayanan, Understanding and control of Zener pinning via phase field and ensemble learning, Comput. Mater. Sci 229 (2023) 112384.
[65] D. Fan, L.Q. Chen, S.P.P. Chen, Numerical simulation of zener pinning with growing second-phase particles, J. Am. Ceram. Soc. 81 (1998) 526–532.
[66] B. AlMangour, Y.-K. Kim, D. Grzesiak, K.-A. Lee, Novel TiB2-reinforced 316L stainless steel nanocomposites with excellent room- and high-temperature yield strength developed by additive manufacturing, Compos. B Eng. 156 (2019) 51–63.
[67] A. Kundu, D.P. Field, Geometrically necessary dislocation density evolution in interstitial free steel at small plastic strains, Metall. Mater. Trans. A 49 (2018) 3274–3282.
[68] A. Sanaty-Zadeh, Comparison between current models for the strength of particulate-reinforced metal matrix nanocomposites with emphasis on consideration of Hall-Petch effect, Mater. Sci. Eng. A 531 (2012) 112–118.
[69] Y.Z. Zhu, S.Z. Wang, B.L. Li, Z.M. Yin, Q. Wan, P. Liu, Grain growth and microstructure evolution based mechanical property predicted by a modified Hall-Petch equation in hot worked Ni76Cr19AlTiCo alloy, Mater. Des. 55 (2014) 456–462.
[70] M.R. Jandaghi, H. Pouraliakbar, Elucidating the microscopic origin of electrochemical corrosion and electrical conductivity by lattice response to severe plastic deformation in Al-Mn-Si alloy, Mater. Res. Bull. 108 (2018) 195–206.
[71] T. Bellezze, G. Giuliani, G. Roventi, Study of stainless steels corrosion in a strong acid mixture. Part 1: cyclic potentiodynamic polarization curves examined by means of an analytical method, Corros. Sci. 130 (2018) 113–125.